J. Astrophys. Astr. (2013) **34,** 393–429

X-ray Observations of Eight Young Open Star Clusters: I. Membership and X-ray Luminosity

Himali Bhatt[1], J. C. Pandey[2], K. P. Singh[3], Ram Sagar[2] & Brijesh Kumar[2]

[1]*Astrophysical Sciences Division, Bhabha Atomic Research Center, Trombay, Mumbai 400 085, India.*
[2]*Aryabhatta Research Institute of Observational Sciences, Manora Peak, Nainital 263 129, India.*
[3]*Tata Institute of Fundamental Research, Mumbai 400 005, India.*
e-mail: mshimali@gmail.com

Received 17 June 2013; accepted 11 November 2013

Abstract. We present a detailed investigation of X-ray source contents of eight young open clusters with ages between 4 to 46 Myr using archival X-ray data from XMM-Newton. The probable cluster memberships of the X-ray sources have been established on the basis of multi-wavelength archival data, and samples of 152 pre-main sequence (PMS) low mass ($<2M_{\odot}$), 36 intermediate mass (2–$10M_{\odot}$) and 16 massive ($>10M_{\odot}$) stars have been generated. X-ray spectral analyses of high mass stars reveal the presence of high temperature plasma with temperature <2 keV, and mean $L_{\rm X}/L_{\rm bol}$ of $10^{-6.9}$. In the case of PMS low mass stars, the plasma temperatures have been found to be in the range of 0.2 keV to 3 keV with a median value of ∼1.3 keV, with no significant difference in plasma temperatures during their evolution from 4 to 46 Myr. The X-ray luminosity distributions of the PMS low mass stars have been found to be similar in the young star clusters under study. This may suggest a nearly uniform X-ray activity in the PMS low mass stars of ages ∼4–14 Myr. These observed values of $L_{\rm X}/L_{\rm bol}$ are found to have a mean value of $10^{-3.6\pm0.4}$, which is below the X-ray saturation level. The $L_{\rm X}/L_{\rm bol}$ values for the PMS low mass stars are well correlated with their bolometric luminosities, that implies its dependence on the internal structure of the low mass stars. The difference between the X-ray luminosity distributions of the intermediate mass stars and the PMS low mass stars has not been found to be statistically significant. Their $L_{\rm X}/L_{\rm bol}$ values, however have been found to be significantly different from each other with a confidence level greater than 99.999% and the strength of X-ray activity in the intermediate mass stars is found to be lower compared to the low mass stars. However, the possibility of X-ray emission from the intermediate mass stars due to

Supplementary material pertaining to this article is available on the *Journal of Astrophysics & Astronomy* website at http://www.ias.ac.in/jaa/dec2013/supp.pdf

a low mass star in close proximity of the intermediate mass star can not be ruled out.

Key words. Open clusters and associations: NGC 663, NGC 869, NGC 884, NGC 7380, Berkeley 86, IC 2602, Trumpler 18, Hogg15—stars: pre-main sequence—X-rays: massive stars, intermediate mass stars, low mass stars.

1. Introduction

Young open star clusters constitute samples of stars of different masses with approximately the same age, distance and chemical composition, and these are homogeneous with respect to these properties. These clusters contain massive ($>10M_{\odot}$), intermediate mass (10–$2M_{\odot}$) and PMS low mass ($<2M_{\odot}$) stars, and therefore, provide useful laboratories to study different mechanisms for the generation of X-rays in stars with different masses. In the massive stars, the X-ray emission arises from shocks in radiatively-driven winds (Lucy & White 1980; Owocki & Cohen 1999; Kudritzki & Puls 2000; Crowther 2007), while in the low-mass stars, rotation with convective envelopes drives a magnetic dynamo leading to strong X-ray emission (Vaiana *et al.* 1981; Güdel 2004). Intermediate mass stars, on the other hand, are expected to be X-ray dark because (a) the wind is not strong enough to produce X-rays as in the case of massive stars (see Lucy & White 1980; Kudritzki & Puls 2000), and (b) being fully radiative internal structure, the dynamo action cannot support the X-ray emission. However, the mysterious detection of X-rays from some intermediate mass stars still remains an open question, and underlying physical mechanisms are not fully known (e.g., Stelzer *et al.* 2006).

Further, the physical origin of X-ray emission from PMS low mass stars is also poorly understood. X-ray studies of low mass PMS stars in young clusters with ages less than 5 Myrs like Orion, IC 348 and NGC 2264 (e.g., see Feigelson *et al.* 2003; Flaccomio *et al.* 2003a, b; Stassun *et al.* 2004; Preibisch *et al.* 2005), and in older Zero-Age-Main Sequence (ZAMS) clusters like the Pleiades and IC 2391 with ages between 30 and 100 Myr (e.g., Micela *et al.* 1999; Jeffries *et al.* 2006; Scholz *et al.* 2007) offer strong evidence that X-ray activity of PMS low mass stars originates due to coronal activity similar to that present in our Sun. Studies of low mass stellar population with different ages, however, show an evolution of the X-ray activity levels in the young stages (<5 Myr), the X-ray luminosity ($L_{\rm X}$) is in the range of 10^{29}–10^{31} erg s^{-1}, compared to much lower activity seen in the older (ZAMS) stars, i.e., $L_{\rm X} \sim 10^{29}$ erg s^{-1}. The X-ray activity is found to decay mildly with age during the evolution of PMS low mass stars from 0.1 to 10 Myr (Preibisch & Feigelson 2005), while it steepens in the Main Sequence (MS) evolution from the ZAMS to a few Gyr age (Feigelson *et al.* 2004). Thus, the evolution of X-ray activity in the PMS stars is somewhat more complicated than in the MS stars. In addition, the ratio of X-ray luminosities to the bolometric luminosity ($L_{\rm X}/L_{\rm bol}$) of PMS low mass stars in young clusters is found to be above the saturation level, i.e., $L_{\rm X}/L_{\rm bol} \approx 10^{-3}$, and uncorrelated with the rotation rates, while the low mass stars in ZAMS clusters show $L_{\rm X}/L_{\rm bol} \sim 10^{-8}$–$10^{-4}$. The stellar X-ray activity deviates from the saturation level for low mass stars in between 1 Myr to 100 Myr (Patten & Simon 1996; Güdel 2004;

Currie *et al.* 2009). However, it is still not clear at which stage of the PMS evolution, the low mass stars deviate from the X-ray saturation level, and which fundamental parameters govern their X-ray emission.

X-ray studies of clusters with intermediate age (5 to 30 Myr) have been few and far between. An extensive study of young open clusters containing a number of stars with a range of masses from massive to PMS low mass stars can address issues specific to the mechanisms producing X-rays in stars with different masses. In addition, the young open clusters with a wide range of ages are also very useful targets for examining the evolution of X-ray emission with age, especially in low mass stars. Multi-wavelength surveys of young open clusters provide an effective way to identify young cluster members among the huge number of foreground and background stars (a few Gyr) present in the same sky region, as young stars are more luminous in X-rays compared to the older field stars (e.g., Micela *et al.* 1985, 1988, 1990; Caillault & Helfand 1985; Stern *et al.* 1981; Preibisch *et al.* 2005).

The present work deals with characterizing the X-ray source contents of eight young open clusters with ages ranging from 4 to 46 Myr. This data sample bridges the gap between young clusters like the Orion and the older clusters like the Pleiades, and constrain the evolution of X-ray emission with age for low mass stars. Samples of massive, intermediate and low mass PMS stars were collected using multi-wavelength archival data. The values of the extinction ($E(B–V)$), distances and age of the open clusters studied here are given in Table 1. The data were taken from XMM-Newton pointed observations of the open clusters NGC 663, NGC 869, NGC 884 and IC 2602, whereas for the clusters NGC 7380, Berkeley 86, Hogg 15 and Trumpler 18, data have been taken from serendipitous observations targeting the massive stars HD 215835, V444 Cyg, WR 47 and supernova remnant SNR MSH11-62, respectively. X-ray emission characteristics of these eight young open clusters have been investigated here for the first time. However, X-ray emission from a few massive stars in the open clusters NGC 7380, Berkeley 86, Hogg 15 and Trumpler 18 have been reported earlier (for details, see §6.1). In addition, previous spectral studies of the X-ray sources in the open cluster NGC 869 (h Persei) have been limited to a region of size $\sim 15'$ (diameter) with Chandra (Currie *et al.* 2009). The present data cover the entire NGC 869 cluster region ($28'$) due to the large field-of-view of the XMM-Newton. The paper is organized as follows: the details of X-ray observations and data reduction procedure are presented in section 2. We have attempted

Table 1. The sample of the clusters under investigation with their basic parameters.

Cluster name	$E(B–V)$ (mag)	N_H* (10^{20} cm^{-2})	Distance (pc)	Age (Myr)	References
NGC 663	0.80±0.15	40±7.5	2400±120	14±1	Pandey *et al.* (2005)
NGC 869	0.55±0.10	28±5	2300±100	13.5±1.5	Currie *et al.* (2010)
NGC 884	0.52±0.10	26±5	2300±100	14±1	Currie *et al.* (2010)
NGC 7380	0.60±0.10	30±5	2600±400	4±1	Chen *et al.* (2011)
Berkeley 86	0.95±0.10	47.5±5	1585±160	6±1	Bhavya *et al.* (2007)
IC 2602	0.035±0.01	1.75±0.5	150±2	46±5	Dobbie *et al.* (2010)
Hogg 15	1.15±0.1	57.5±5	3000±300	6±2	Sagar *et al.* (2001)
Trumpler 18	0.3±0.04	15±0.2	1300±100	30±15	Delgado *et al.* (2007)

*N_H is derived using the relation $N_H = 5 \times 10^{21} \times E(B–V)$ cm^{-2} from Vuong *et al.* (2003).

to ascertain the cluster probable membership of X-ray sources in section 3. X-ray variability and spectra of the cluster members are presented in sections 4 and 5, respectively. The X-ray properties of cluster members are discussed in section 6 and results are summarized in section 7.

2. X-ray observations and data reduction

XMM-NEWTON carries three co-aligned X-ray telescopes observing simultaneously, and covering $30' \times 30'$ region of the sky. It consists of three CCD-based detectors: the PN CCD (Strüder *et al.* 2001) and the twin CCD detectors MOS1 and MOS2 (Turner *et al.* 2001). EPIC has moderate spectral resolution ($\frac{E}{\delta E} \sim 20$–50) and an angular resolution[1] of $4.5''$, $6.0''$ and $6.6''$ for PN, MOS1 and MOS2 detectors, respectively. It together constitutes the European Photon Imaging Camera (EPIC). We have analysed archival X-ray data from XMM-NEWTON observations of eight young open clusters and the journal of observations is given in Table 2. All three EPIC detectors were active at the time of observations with full frame mode. Data reduction followed the standard procedures using the XMM-NEWTON Science Analysis System software (SAS version 10.0.0) with updated calibration files. Event files for MOS and PN detectors were generated by using tasks EMCHAIN and EPCHAIN, respectively, which allow calibration, both in energy and astrometry, of the events registered in each CCD chip and combine them in a single data file. We limited our analysis to the energy band to 0.3–7.5 keV because data below 0.3 keV are mostly unrelated to bona-fide X-rays, while above 7.5 keV only background counts are present, for the kind of sources that we are interested in. Event list files were extracted using the SAS task EVSELECT. Data from the three cameras were individually screened for high background periods and those time intervals were excluded where the total count rate (for single events of energy above 10 keV) in the instruments exceed 0.35 and 1.0 counts s^{-1} for the MOS and PN detectors, respectively. The useful exposure times, i.e., sum of good time intervals, obtained after screening the high background periods for each cluster and corresponding to each detector used, are given in Table 2.

2.1 *Detection of X-ray point sources*

Detection of point sources is based on the SAS detection task EDETECT_CHAIN, which is a chain script of various sub tasks (for details, see XMM documentation[2]). First, the input images were built in two energy ranges, a soft band (0.3–2.0 keV) and a hard band (2.0–7.5 keV) for all three EPIC detectors with a pixel size of $2''.0$, corresponding to a bin size of 40 pixels in the event file where each pixel size corresponds to $0''.05$. The task EDETECT_CHAIN was then used simultaneously on these images. This task determined the source parameters (e.g., coordinates, count rates, hardness ratios, etc.) by means of simultaneous maximum likelihood psf (point spread

[1] http://heasarc.gsfc.nasa.gov/docs/xmm/uhb/onaxisxraypsf.html
[2] http://xmm.esac.esa.int/sas/current/documentation/threads/src_find_thread.shtml

Table 2. Journal of XMM-Newton observations of eight young clusters.

Cluster name	Observation ID	Exposure time (sec)	Start time UT (hh:mm:ss)	Final retained exposure time MOS1 (ks)	MOS2 (ks)	PN (ks)	EPIC filter	Offset from target (arcmin)
NGC 663	0201160101	41915	14 Jan 2004 22:40:26	32.59	33.13	28.69	Medium	1.606
NGC 869	0201160201	39509	19 Jan 2004 04:39:50	38.50	38.32	34.88	Medium	1.871
NGC 884	0201160301	40620	04 Feb 2004 15:13:25	33.08	33.73	26.08	Medium	1.013
NGC 7380	0205650101	31413	19 Dec 2003 02:02:12	25.23	25.46	19.52	Thick	3.621
Berkeley 86	0206240801	19921	27 Oct 2004 23:25:39	18.86	18.79	15.11	Thick	8.807
IC 2602	0101440201	44325	13 Aug 2002 05:10:42	36.47	36.69	31.87	Medium	5.550
Hogg 15	0109480101	53040	03 July 2002 15:51:56	48.30	52.08	51.80	Thick	4.509
Trumpler 18*	0051550101	40822	06 Feb 2002 01:13:19		35.85	39.20	Medium	3.968

*The observations have not been done in prime full window mode for MOS1 detector.

function) fitting to the source count distribution in the soft and the hard energy bands of each EPIC instrument. A combined maximum likelihood value in all three instruments was taken to be greater than 10, corresponding to a false detection probability of $\approx 4.5 \times 10^{-5}$. The output source lists from the individual EPIC cameras in different energy bands were merged into a common list and the average values for the source positions with count rates were calculated. The final output list was thus created giving source parameters for the soft and the hard energy bands along with the total energy band of 0.3–7.5 keV. Spurious detections due to inter-chip gaps between CCDs, the hot pixels and the surroundings of bright point source regions have been removed by visual screening. Finally, the number of X-ray sources detected in NGC 663, NGC 869, NGC 884, NGC 7380, Berkeley 86, IC 2602, Hogg 15 and Trumpler 18 were 85, 183, 147, 88, 95, 95, 124 and 208, respectively. The estimated positions of the all X-ray point sources along with their count rates in the total energy band of 0.3–7.5 keV are listed in Table 3. Each source has been ascribed a unique Identification Number (ID) which is also given in supplementary material.

The count rate of an X-ray source detected using EDETECT_CHAIN task with 2σ significance and lying within the cluster radius has been considered as the detection limit for each cluster. These detection limits in terms of count rates have been converted into flux limits using the Count Conversion Factors (CCFs) used for low mass stars (see section 5) and corresponding X-ray luminosities have been tabulated in Table 4 for each cluster.

2.2 *Infrared counterparts of X-ray sources*

X-ray point sources detected in the clusters were cross-identified with NIR sources listed in the Two-Micron All Sky Survey (2MASS) Point Source Catalog (PSC; Cutri *et al.* 2003). The X-ray counterparts in the 2MASS catalogue were then searched for within a radius of $10''$, only those with a 'read flag' (representing uncertainties in their magnitude) value of 1 or 2 were retained. In several cases, multiple counterparts are possible in the 2MASS PSC corresponding to an X-ray source and the number of multiple counterparts are given in column 9 (N) in supplementary material. In such cases, NIR sources that are closest to an X-ray source have been adopted as corresponding counterparts of that source. The JHK_S magnitudes, the positions of the X-ray sources from the center of the corresponding open cluster (see section 3), and the offsets between the X-ray and the NIR positions of the NIR counterparts are given in supplementary material. It was thus found that only 70%, 77%, 70%, 86%, 94%, 78%, 85% and 93% of the X-ray sources in the open clusters NGC 663, NGC 869, NGC 884, NGC 7380, Berkeley 86, IC 2602, Hogg 15 and Trumpler 18, respectively, have 2MASS NIR counterparts. Optical spectroscopic catalogues of stars from Webda[3] and Vizier[4] were used for the optical identification of X-ray sources (see supplementary material).

[3] http://www.univie.ac.at/webda/navigation.html
[4] http://vizier.u-strasbg.fr/viz-bin/VizieR

Table 3. X-ray information of all detected sources in detection procedure (for details see section 2.1) within the field-of-view of XMM-NEWTON along with their cross-identification with the 2MASS infrared catalogue (Cutri *et al.* 2003).

Please note that Table 3 presented here is just a sample. The complete Table 3 can be viewed at the following site (http://www.ias.ac.in/jaa/dec2013/supp.pdf)

	X-ray data							2MASS NIR data						Mem	Mass	Remark
ID	RA	DEC	Err	Count rates 10^{-3} cts s^{-1}			Dis	N	Off	J	H	K_s			($M_\odot$)	
	(deg)	(deg)	($''$)	PN	MOS1	MOS2	($'$)		($''$)	(mag)	(mag)	(mag)				
1	2	3	4	5	6	7	8	9	10	11	12	13	14	15	16	
NGC 663																
1	26.177084	61.141083	1.3	0.0±0.0	1.8±0.5	1.5±0.5	13.7	2	0.8	13.597±0.023	13.071±0.035	12.889±0.037	Y	<2.0		
2	26.251165	61.158890	1.7	1.7±0.6	0.8±0.3	1.5±0.4	11.3	1	2.1	15.082±0.043	14.579±0.058	14.338±0.079				
⋮	⋮	⋮	⋮	⋮	⋮	⋮	⋮	⋮	⋮	⋮	⋮	⋮	⋮	⋮		

Notes – 1: Identification number of X-ray sources detected using SAS task EDETECT_CHAIN.
2: Right ascension of source in units of degree at J2000 epoch.
3: Declination of source in units of degree at J2000 epoch.
4: Error in the estimation of position from X-ray source detection algorithm in units of arcsec.
5: Count rates are estimated in energy band 0.3–7.5 keV from SAS task EDETECT_CHAIN in PN detector.
6: Count rates are estimated in energy band 0.3–7.5 keV from SAS task EDETECT_CHAIN in MOS1 detector.
7: Count rates are estimated in energy band 0.3–7.5 keV from SAS task EDETECT_CHAIN in MOS2 detector.
8: Distances of the source from the center of the cluster in units of arcmin.
9 : Number of multiple identifications of a X-ray source in 2MASS NIR source catalogue within 10$''$search radius.
10: Distance (in arcsec) between the positions of the X-ray source and of its closest NIR within 10$''$search radius. Only the closest identification of the X-ray source has been reported in this table.
11: Magnitudes of the closest X-ray counterparts in J (1.25 μm) band.
12: Magnitudes of the closest X-ray counterparts in H (1.65 μm) band.
13: Magnitudes of the closest X-ray counterparts in K_s (2.17 μm) band.
14: Membership of X-ray source in their corresponding cluster.'Y' represents the cluster member while 'N' represents non-member.
15: Masses of the sources estimated from color-magnitude diagrams of the clusters for cluster members in units of $M_\odot$.
16: The information of the source from Vizier database. the references are: Sk07 represents Skiff (2007); Cu10 represents Currie *et al.* (2010); S02 represents Slesnick *et al*. (2002); S05 represents Strom *et al.* (2005); Pic10 represents Pickles & Depagne (2010); Ogu02 represents Ogura *et al.* (2002); Ike08 represents Ikeda *et al.* (2008); Glebocki05 represents Glebocki & Gnacinski (2005); D'orazi09 represents D'Orazi & Randich (2009); Delgado11 represents Delgado *et al.* (2011); Kher09 represents Kharchenko & Roeser (2009); Fab02 represents Fabricius *et al*. (2002). The probability of the X-ray source for being a star is given from Flesch (2010; Fl10).

Table 4. Detection fraction of X-ray sources within cluster radius with a comparison of radius of the clusters derived using NIR data and optical data.

Cluster name	Center 2MASS		Radius		No. of X-ray sources				Detection limits[2]
					Detected		Identified		
	RA_{J2000}	DEC_{J2000}	Dias02[1]	2MASS	Total	Cluster	Total	Cluster	$\log(L_X)$
	hh:mm:ss	hh:mm:ss	(′)	(′)					erg s^{-1}
NGC 663	01:46:29	+61:13:05	7	15	85	84	60	32	30.43
NGC 869	02:19:00	+57:08:57	9	14	183	181	141	78	30.24
NGC 884	02:22:04	+57:08:49	9	11	147	114	103	71	30.36
NGC 7380	22:47:47	+58:07:15	10	8	88	40	76	37	30.85
Berkeley 86	20:20:22	+38:42:07	3	3.5	96	11	90	11	30.62
IC 2602	10:43:06	−64:25:30	50	–	95	95	74	74	27.57
Hogg 15	12:43:39	−63:05:58	3.5	7	124	53	106	47	30.70
Trumpler 18	11:11:31	−60:40:41	2.5	–	208	11	194	10	29.75

[1]Radius derived using optical data in literature (Dias *et al.* 2002).
[2]2σ detection limits of observations are derived from count rate conversion into flux in PN detector for low mass stars (see §4).

3. Cluster membership of X-ray sources

The X-ray sources with identifiable counterparts in the NIR band may not necessarily be members of their respective clusters. It is difficult to decide cluster membership of an individual X-ray source, because the cluster population is contaminated by foreground and background stellar sources (Pizzolato *et al.* 2000) and extragalactic sources (Brandt & Hasinger 2005). In order to find which of the X-ray sources actually belong to a cluster, the approach given by Currie *et al.* (2010) has been adopted here. The step by step procedure used is given below.

3.1 *Center and radius of the clusters*

The stellar population associated with young open clusters is still embedded in parent molecular clouds, due to which a large variation in extinction is found within young open clusters. The young stars embedded within high extinction regions of the cluster and hidden in the optical bands may be visible in the NIR band. Therefore, NIR data from the 2MASS PSC (Cutri *et al.* 2003) were used to estimate the center of these clusters and their extents rather than the optical data. The center of a cluster was first taken to be an eye estimated center of the cluster and then refined as follows. The average RA(J2000) and DEC(J2000) position of 2MASS stars having $K_S \leq 14.3$ mag (99% completeness limit in K_S band) and lying within $1'$ radius was computed. The average RA(J2000) and DEC(J2000) were reestimated by using this estimated value of the center of the cluster. This iterative method was used until it converged to a constant value for the center of the open cluster (see Joshi *et al.* 2008 for details). Typical error expected in locating the center by this method is $\sim 5''$. The estimated values of the center of each open cluster are given in Table 4. The positions of the centers estimated from the NIR data are consistent within $1'$ to that estimated from the optical data by Dias *et al.* (2002). Assuming spherical symmetry for the cluster, a projected radial stellar density profile of stars was constructed and the radius at which the stellar density is at the 3σ level above the field star density was determined. The field star densities were estimated from the 200 arcmin^2 region which is nearly more than 0.5 degree away from the cluster regions. The estimated values of field star densities are 2.21 ± 0.10, 1.95 ± 0.10, 1.95 ± 0.10, 2.86 ± 0.12, 6.91 ± 0.18 and 13.14 ± 0.26 stars arcmin^{-2} for the clusters NGC 663, NGC 869, NGC 884, NGC 7380, Berkeley 86 and Hogg 15, respectively. The estimated values of the radii of the open clusters are given in Table 4. We have adopted the estimated radii, reported in Table 4, as a measure of the extent of the open clusters. Our estimates of the radii of the clusters are larger than that of the values given by Dias *et al.* (2002) using optical data except for the open cluster Berkeley 86. However, these values are consistent with the values given by Pandey *et al.* (2005) and Currie *et al.* (2010) in the case of NGC 663 and NGC 869, respectively. It is not possible to define the cluster extent in the case of IC 2602 and Trumpler 18 because the boundary where the stellar densities merge into field star densities is not clearly marked in the radial density profiles. This may be either due to the very large size of the cluster in the case of IC 2602, and very small size in the case of Trumpler 18, or the stars in the clusters may not be distributed in a spherical symmetry. For further analysis, we used the radii given in Dias *et al.* (2002) catalogue for these two open clusters. The projected distances of X-ray sources from the center of the respective clusters are given in supplementary material. The

number of X-ray sources within the radius of cluster are also given in Table 4. All the X-ray sources with a counterpart in NIR and falling within the adopted radius of the corresponding cluster have been considered for further analysis to check if they are members of that cluster.

3.2 *Color-magnitude diagram of X-ray sources with NIR counterparts*

Assigning cluster membership to X-ray sources is a difficult task. It is, however, easier to check if an X-ray source lying within the cluster radius is not a member by using Color Magnitude Diagrams (CMDs). In Fig. 1, we plot the CMDs using the 2MASS J magnitudes and $(J - H)$ colors of the sources selected in section 3.1 and lying within the cluster radii. We define the fiducial locus of cluster members for each open cluster by the post-main sequence isochrones from Girardi *et al.* (2002) and PMS isochrones from Siess *et al.* (2000) according to their ages, distances and mean reddening (see Table 1). These locii have been shown by dashed lines in Fig. 1. Width of each of the cluster locii has been determined by (1) uncertainties in the determination of distance and age of the cluster, (2) uncertainties in the photometric 2MASS J and H magnitudes of the sources which is higher at the fainter end, (3) dispersion in the reddening, and (4) binarity. Equal mass binaries may be up to 0.75 mag more luminous than single stars. The X-ray sources which are lying outside this fiducial locus for a given cluster are excluded from being members in that cluster. The number of stars thus excluded from being members are 10, 22, 11, 9, 2, 42, 14 and 2, in the open clusters NGC 663, NGC 869, NGC 884, NGC 7380, Berkeley 86, IC 2602, Hogg 15 and Trumpler 18, respectively.

The remaining X-ray sources were further screened for probable membership of the respective open clusters. Each of these X-ray source was investigated on the basis of information given in the optical spectroscopic catalogues from Vizier services. This spectroscopic information with references is given in supplementary material. The sources for which the spectroscopic characteristics did not match with their photometric location in the CMDs were no longer considered for membership of the corresponding cluster, and thus removed from the list of probable members. This method is useful for removing the foreground contamination. However, background contamination is very difficult to separate. Therefore, we have further cross-identified these selected sources in the all-sky comprehensive catalogue of radio and X-ray associations by Flesch (2010), in which the probability of a source being a quasi stellar object (QSO), a galaxy or a star has been given. Those sources for which the probability for being a star is less than 20% were also removed from the list of selected sources. Using this method, the number of additional X-ray sources that are no longer considered as members of the open clusters NGC 663, NGC 869, NGC 884, NGC 7380, Berkeley 86, IC 2602 and Hogg 15 were 5, 1, 3, 2 , 1, 2 and 1, respectively.

The X-ray sources that are no longer considered as members of a cluster are marked by the symbol of a cross in Fig. 1 and listed as 'N' in supplementary material (column 14). The remaining X-ray sources are considered to be the probable members of their respective clusters. We could thus assign probable cluster membership for 21, 70, 34, 25, 8, 10, 30 and 6 X-ray sources in clusters NGC 663, NGC 869, NGC 884, NGC 7380, Berkeley 86, IC 2602, Hogg 15 and Trumpler 18, respectively,

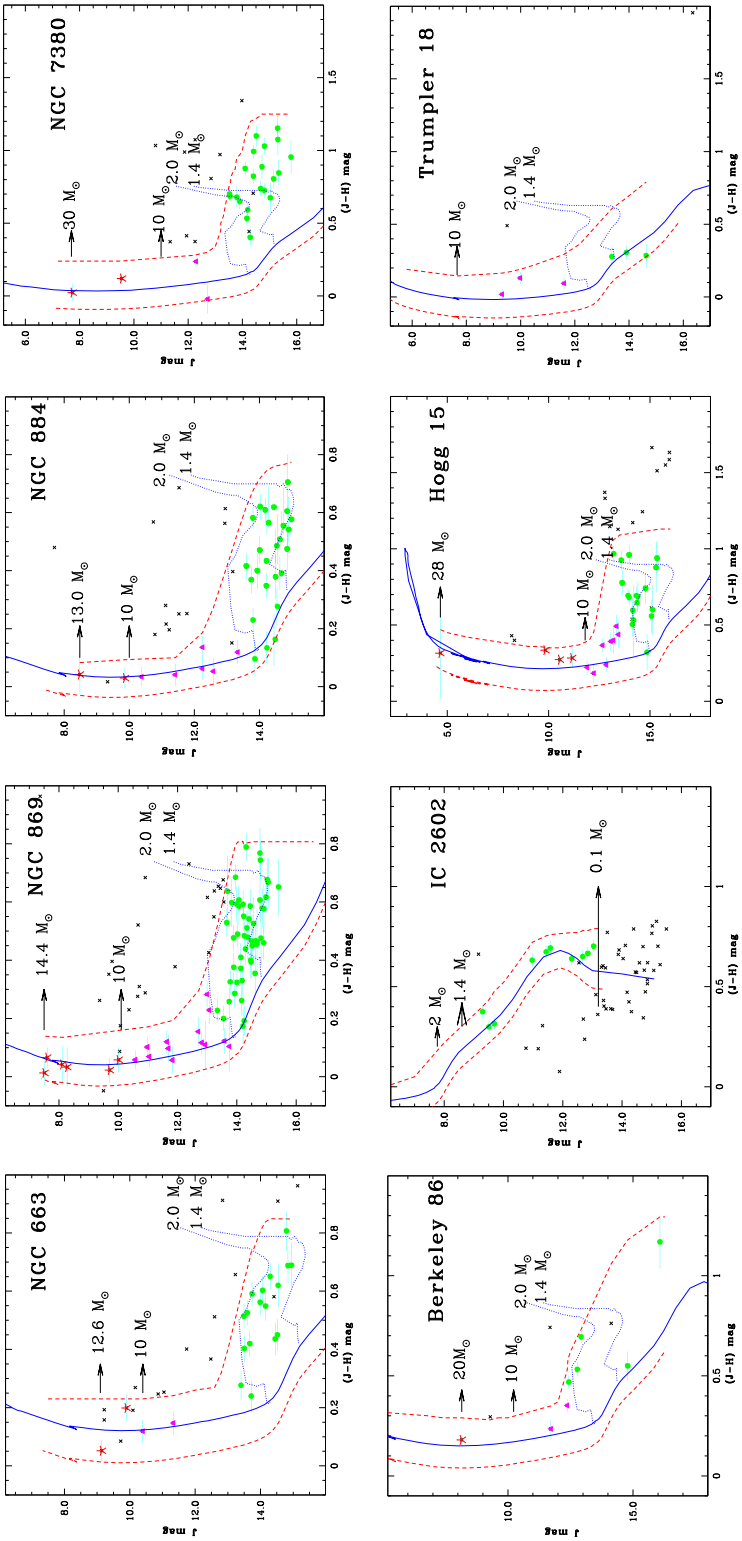

Figure 1. J versus $(J-H)$ color magnitude diagram (CMD) of the X-ray sources within cluster radius. Post-main sequence isochrones from Girardi *et al.* (2002) and PMS isochrones from Siess *et al.* (2000) are shown by solid and dotted lines (in blue). The width of the cluster locus due to uncertainties in determination of distance, age, magnitudes and binarity is shown by dashed lines (in red). The symbols of star, triangle and dots represent massive, intermediate and low mass stars, respectively, and these boundaries are marked by arrows. The X-ray sources identified as a non-member of their respective open clusters are marked by the symbol of a cross.

and listed as 'Y' in supplementary material (column 14). Further, proper-motion and/or spectroscopic studies are needed to confirm the membership of specific X-ray sources. However, proper motions at a distance of 2.0 kpc are extremely hard to detect. X-ray sources lying outside the cluster radius remain as unclassified.

3.3 *Mass estimation of X-ray stars*

The masses of X-ray stars, identified as probable members of the clusters, were estimated using theoretical isochrones of Girardi *et al.* (2002) for MS stars and Siess *et al.* (2000) for PMS stars. The boundaries corresponding to a $10M_{\odot}$ (massive) star, 10–$2M_{\odot}$ (intermediate mass) star and a $2M_{\odot}$ (low mass) star were derived from the J magnitudes using model isochrones corrected for distance, age and reddening for each cluster, and are shown in Fig. 1 by arrows. The estimated mass of each star identified as a probable member is given in supplementary material. In Fig. 1, the massive stars, intermediate mass stars and low mass stars are marked by the symbols of star, triangle and dots, respectively.

4. Variability of X-ray sources

X-ray emission of stars is known to be variable, and before estimating their luminosity function it is important to first study their variability. Due to its highest sensitivity, data from the PN detector of EPIC were used for variability and spectral analysis. Light curves and spectra for all the probable members were extracted using circular extraction regions centered on the source position provided by EDETECT_CHAIN task in the energy range of 0.3–7.5 keV. X-ray sources either falling in the inter-chip gaps in the PN detector or having total counts below 40 in the PN detector were ignored for variability and spectral analyses. The wings of the psf for bright sources are often largely contaminated by emission from neighboring sources, therefore, the radii of extraction regions were varied between $8''$ and $40''$ depending on the position of the source in the detector and its angular separation with respect to the neighboring X-ray sources. The background data were taken from several neighboring source-free regions on the detectors. For the timing analysis, we have binned the data with 300–5000 s according to the count rate of the sources. Due to poor count statistics, there were several time intervals in which count rates were lesser than 5, therefore, we were not able to perform the χ^2-test for variability analysis. Fractional root mean square (rms) variability amplitude ($F_{\rm var}$) was estimated to quantify the variability in the X-ray light curves for intermediate and low mass stars. The $F_{\rm var}$ and the error in $F_{\rm var}$ ($\sigma_{F_{\rm var}}$) have been defined as follows (Edelson *et al.* 1990, 2002) and given in Table 5:

$$F_{\rm var} = \frac{1}{\langle X \rangle}\sqrt{S^2 - \langle \sigma_{\rm err}^2 \rangle}, \tag{1}$$

$$\sigma_{F_{\rm var}} = \frac{1}{F_{\rm var}}\sqrt{\frac{1}{2N}}\frac{S^2}{\langle X \rangle^2}, \tag{2}$$

where S^2 is the total variance of the light curve, $\langle \sigma_{\rm err}^2 \rangle$ is the mean error squared and $\langle X \rangle$ is the mean count rate, however, $F_{\rm var}$ can not be defined when S^2 is lesser than $\langle \sigma_{\rm err}^2 \rangle$. $F_{\rm var}$ quantifies the amplitude of variability with respect to the mean count rate.

Table 5. Spectral and timing properties of intermediate and low mass stars in young open clusters.

Cluster name	Source detection ID	RA_{J2000} (deg)	DEC_{J2000} (deg)	kT (keV)	Spectral log(EM) (cm^{-3})	log(L_X)† (ergs s^{-1})	log($\frac{L_X}{L_{bol}}$)	Timing Bin size (s)	F_{var}
Intermediate mass stars (2–10 $M_\odot$)									
NGC663	42	26.583460	61.263973	>2.78	$53.81^{+0.14}_{-0.18}$	31.02	−6.47		
NGC663	48	26.604250	61.208221	>1.79	$53.85^{+0.15}_{-0.19}$	30.98	−6.01		
NGC869	10	34.441750	57.088139			30.70	−5.75		
NGC869	13	34.457584	57.318527			31.26	−4.75		
NGC869	17	34.481415	57.218498			30.98	−6.08		
NGC869	21	34.512001	57.076889			30.51	−4.43		
NGC869	64	34.647793	57.214417			30.81	−4.91		
NGC869	67	34.662083	57.220444	$0.54^{+0.43}_{-0.33}$	$53.42^{+0.56}_{-0.32}$	30.48	−4.35	800	0.89±0.17
NGC869	69	34.671417	57.102196	$2.75^{+14.10}_{-1.45}$	$54.03^{+0.16}_{-0.21}$	31.10	−3.50		
NGC869	88	34.750916	57.154499			30.51	−6.47		
NGC869	105	34.783291	57.127804	$3.10^{+2.50}_{-1.10}$	$54.01^{0.10}_{-0.10}$	31.11	−4.55		
NGC869	139	34.869793	57.154026	$1.95^{+1.96}_{-0.62}$	$54.06^{+0.09}_{-0.11}$	31.09	−6.16		
NGC869	140	34.870708	57.163887	$1.27^{+0.43}_{-0.23}$	$53.98^{+0.13}_{-0.15}$	31.04	−5.42	800	0.72±0.14
NGC869	169	35.026749	57.125500			30.70	−6.53		
NGC869	173	35.037834	57.020638	$2.80^{+2.30}_{-0.80}$	$54.34^{0.08}_{-0.10}$	31.52	−5.04		
NGC884	23	35.328167	57.146667	>3.80	$54.12^{+0.20}_{-0.09}$	31.33	−4.84	1100	0.13±0.47
NGC884	62	35.461918	57.026669	>3.26	$53.90^{+0.22}_{-0.17}$	31.10	−5.08		
NGC884	68	35.489666	57.211613			<30.52	< −6.22		
NGC884	78	35.517044	57.142250			30.81	−5.12		
NGC884	103	35.613209	57.054779	$1.30^{+0.31}_{-0.23}$	$54.00^{+0.11}_{-0.14}$	31.04	−6.29		
NGC884	120	35.707790	57.142834	>15.80	$54.06^{+0.13}_{-0.24}$	31.16	−4.18		
NGC7380	51	341.83798	58.088665			30.99	−5.44		
NGC7380	59	341.89688	58.125500	$2.38^{+1.43}_{-0.65}$	$54.59^{+0.08}_{-0.09}$	31.65	−4.45		

Table 5. (*Continued*).

Cluster name	Source detection			kT (keV)	Spectral			Timing	
	ID	RA_{J2000} (deg)	DEC_{J2000} (deg)		log(EM) (cm^{-3})	$\log(L_X)^{\dagger}$ (ergs s^{-1})	$\log(\frac{L_X}{L_{bol}})$	Bin size (s)	F_{var}
Berkeley 86	76	305.04416	38.695137	$1.36^{+0.70}_{-0.31}$	$53.74^{+0.17}_{-0.20}$	30.47	−5.80		
Berkeley 86	79	305.00755	38.680832	Not fitted with model					
Hogg15	11	190.79124	−63.003056	$0.14^{+0.62}_{-0.05}$	>56.95	32.57	−4.44		
Hogg15	33	190.89438	−63.014778	$0.28^{+0.66}_{-0.10}$	>55.45	31.73	−4.86		
Hogg15	34	190.98633	−63.081444	$1.55^{+0.27}_{-0.24}$	$54.80^{+0.06}_{-0.06}$	31.76	−5.46		
Hogg15	42	190.96179	−63.113388	$0.16^{+0.12}_{-0.05}$	>56.17	32.13	−4.09		
Hogg15	48	190.98618	−63.071609	$0.18^{+0.05}_{-0.03}$	$55.44^{+0.38}_{-0.36}$	32.19	−4.15		
Hogg15	55	191.00912	−63.067471			31.71	−5.01		
Hogg15	65	191.06125	−63.137749	$0.69^{+0.26}_{-0.22}$	$54.20^{+0.16}_{-0.17}$	31.30	−4.85	4800	0.69±0.33
Hogg15	82	191.15871	−63.086193	>6.27	$54.39^{+0.12}_{-0.19}$	31.56	−4.87		
Trumpler 18	76	167.88104	−60.664612	$6.99^{+50.8}_{-3.61}$	$53.53^{+0.08}_{-0.09}$	30.70	−4.50		
Trumpler 18	80	167.89404	−60.667278	$5.63^{+13.8}_{-2.82}$	$54.21^{+0.08}_{-0.08}$	31.38	−4.77		
Trumpler 18	90	167.92091	−60.706276	$0.84^{+0.12}_{-0.08}$	$53.71^{+0.05}_{-0.06}$	30.81	−5.75		
Low mass stars ($<2M_{\odot}$)									
NGC663	1	26.177084	61.141083			31.23	−4.17		
NGC663	4	26.284582	61.317722			30.98	−4.02		
NGC663	7	26.319500	61.133999			30.79	−4.28		
NGC663	8	26.320749	61.281723			31.33	−4.15		
NGC663	12	26.358292	61.181416			30.98	−4.58		
NGC663	15	26.378542	61.141777			31.36	−3.57		
NGC663	17	26.385792	61.345470			30.96	−3.68		
NGC663	18	26.390625	61.064499			30.95	−3.59		
NGC663	41	26.582500	61.229389			30.93	−4.37		
NGC663	52	26.639708	61.056168			30.85	−3.41		
NGC663	56	26.663834	61.150028	$0.27^{+0.02}_{-0.02}$	$55.29^{+0.09}_{-0.07}$	32.16(?)	−2.01(?)	500	0.10±0.23

Table 5. (*Continued*).

Cluster name	Source detection			Spectral				Timing	
	ID	RA_{J2000} (deg)	DEC_{J2000} (deg)	kT (keV)	log(EM) (cm^{-3})	$\log(L_X)^{\dagger}$ (ergs s^{-1})	$\log(\frac{L_X}{L_{bol}})$	Bin size (s)	F_{var}
NGC663	61	26.689041	61.107445	>9.66	$54.35^{+0.08}_{-0.18}$	31.46(?)	−1.84(?)		
NGC663	66	26.729250	61.048973			31.14	−3.42		
NGC663	80	26.941376	61.183498	>9.37	$54.64^{+0.11}_{-0.12}$	31.78	−3.69	2000	0.26±0.18
NGC663	81	26.983583	61.209415			31.57	−3.24		
NGC663	82	27.015417	61.212749	$1.36^{+0.79}_{-0.38}$	$54.15^{+0.16}_{-0.19}$	31.17	−4.17		
NGC663	83	27.019709	61.118973	$0.50^{+0.29}_{-0.31}$	$54.74^{+0.79}_{-0.26}$	31.76	−3.52	3500	0.54±0.40
NGC869	1	34.341042	57.174751			31.16	−2.96		
NGC869	19	34.498043	56.965668			31.01	−3.85		
NGC869	20	34.511124	57.110722			30.54	−3.51		
NGC869	22	34.518623	57.345470			30.91	−3.92		
NGC869	23	34.522251	57.024361			30.65	−3.40		
NGC869	25	34.530666	57.207554			30.57	−3.96		
NGC869	33	34.557877	57.297722			30.65	−4.03		
NGC869	34	34.559208	57.030613			30.78	−4.18		
NGC869	36	34.571877	57.125416	$0.97^{+0.65}_{-0.19}$	$53.85^{+0.12}_{-0.14}$	30.95	−3.16		
NGC869	40	34.584126	57.273140			30.60	−3.36		
NGC869	41	34.585751	57.109943			31.03	−3.46		
NGC869	42	34.586708	57.174110	$3.66^{+14.00}_{-1.90}$	$54.25^{+0.11}_{-0.12}$	31.38	−3.18	600	0.47±0.10
NGC869	44	34.595165	57.182278	$2.47^{+3.82}_{-0.85}$	$53.86^{+0.12}_{-0.14}$	30.93	−3.36		
NGC869	47	34.603626	57.112083			30.47	−3.87		
NGC869	58	34.628918	57.064999	>2.21	$53.65^{+0.28}_{-0.24}$	30.86	−3.05		
NGC869	61	34.633835	57.248390			30.65	−4.51		
NGC869	68	34.668709	57.127224			30.67	−3.59		
NGC869	73	34.696793	56.956944			31.09	−3.08		
NGC869	74	34.701958	57.074444	$1.25^{+0.77}_{-0.27}$	$53.75^{+0.15}_{-0.16}$	30.80	−4.53	3000	0.20±0.55
NGC869	75	34.703083	57.121082	$2.60^{+1.90}_{-0.75}$	$54.11^{+0.08}_{-0.09}$	31.19	−3.85		

Table 5. (*Continued*).

Cluster name	Source detection				Spectral			Timing	
	ID	RA_{J2000} (deg)	DEC_{J2000} (deg)	kT (keV)	log(EM) (cm^{-3})	$\log(L_X)^{\dagger}$ (ergs s^{-1})	$\log(\frac{L_X}{L_{bol}})$	Bin size (s)	F_{var}
NGC869	78	34.717876	57.192001	$3.30^{+7.45}_{-1.38}$	$53.84^{+0.13}_{-0.15}$	29.69	−4.46		
NGC869	79	34.719166	57.074360			30.44	−3.86		
NGC869	92	34.754833	57.003334	>2.28	$54.04^{+0.12}_{-0.13}$	31.24	−3.82		
NGC869	93	34.754959	57.097694			30.85	−3.83		
NGC869	96	34.759666	57.160721	$3.00^{+3.94}_{-1.30}$	$54.07^{+0.10}_{-0.12}$	31.17	−3.82	2000	0.31±0.27
NGC869	99	34.768124	57.160999	$2.42^{+2.27}_{-0.90}$	$54.07^{+0.09}_{-0.10}$	31.13	−3.27	1000	0.45±0.21
NGC869	104	34.782333	57.102638	>1.89	$53.83^{+0.13}_{-0.16}$	30.98	−3.23		
NGC869	108	34.790833	57.153000			30.35	−4.18		
NGC869	111	34.794624	57.125721					600	0.64±0.09
NGC869	113	34.801960	57.064667	$0.23^{+0.05}_{-0.04}$	$54.40^{+0.21}_{-0.17}$	31.25	−3.67		
NGC869	114	34.807625	57.030193	$1.71^{+1.25}_{-0.520}$	$53.79^{+0.14}_{-0.20}$	30.80	−3.24		
NGC869	115	34.812290	57.218582			30.80	−3.22		
NGC869	121	34.824207	57.134972			30.35	−4.03		
NGC869	123	34.830917	57.202499			30.68	−3.93		
NGC869	128	34.839500	57.034805			30.90	−3.34		
NGC869	129	34.841667	57.232334			30.57	−3.30		
NGC869	132	34.848293	57.025417			30.72	−3.79		
NGC869	135	34.854874	56.991890	$0.99^{+0.73}_{-0.64}$	$54.07^{+0.15}_{-0.17}$	31.17	−3.60		
NGC869	143	34.883999	57.113998			30.54	−4.32		
NGC869	145	34.890583	57.059082	$0.73^{+0.28}_{-0.27}$	$53.60^{+0.15}_{-0.19}$	30.72	−3.24		
NGC869	146	34.890751	57.258167			30.51	−4.10		
NGC869	149	34.91346	57.060806			30.51	−4.22		
NGC869	152	34.929249	57.312527			30.83	−3.16		
NGC869	155	34.947918	57.151196			31.20	−3.38		
NGC869	156	34.952667	57.039165	$4.40^{+12.0}_{-1.90}$	$54.12^{+0.10}_{-0.12}$	31.28	−3.21		
NGC869	158	34.960876	57.251278			30.81	−3.64		

Table 5. (*Continued*).

Cluster name	Source detection ID	RA_{J2000} (deg)	DEC_{J2000} (deg)	kT (keV)	Spectral log(EM) (cm^{-3})	log(L_X)† (ergs s^{-1})	log($\frac{L_X}{L_{bol}}$)	Timing Bin size (s)	F_{var}
NGC869	159	34.961082	57.199333	$2.14^{+2.54}_{-0.69}$	$54.09^{+0.10}_{-0.12}$	31.12	−3.31		
NGC869	162	34.980000	57.220444	$0.93^{+0.30}_{-0.47}$	$53.80^{+0.14}_{-0.17}$	30.96	−3.85		
NGC869	165	34.999458	57.253887			30.74	−4.01		
NGC869	166	35.011665	57.318638			31.15	−2.52		
NGC869	174	35.071041	57.147530			30.93	−2.95		
NGC869	175	35.083668	57.010471			<30.65	<−3.78		
NGC884	16	35.268585	57.129139			30.56	−4.26		
NGC884	28	35.357166	57.050220			30.59	−4.16		
NGC884	30	35.369831	57.103806	$1.06^{+0.42}_{-0.35}$	$53.77^{+0.44}_{-0.35}$	30.75	−3.71		
NGC884	39	35.409168	57.068306			30.47	−3.76		
NGC884	49	35.434875	57.264473			30.74	−3.53		
NGC884	53	35.442039	57.044498	>0.70	<54.45	30.94	−3.37		
NGC884	64	35.466541	57.276859	$2.40^{+5.20}_{-0.94}$	$54.00^{+0.14}_{-0.17}$	31.07	−2.84		
NGC884	71	35.503956	57.079613	>4.26	$54.06^{+0.17}_{-0.09}$	31.27	−3.67		
NGC884	75	35.512707	57.308529			31.09	−3.13		
NGC884	80	35.524750	57.118694			30.50	−4.39		
NGC884	88	35.552002	57.100750	$1.65^{+0.68}_{-0.31}$	$54.15^{+0.09}_{-0.10}$	31.17	−2.81	2200	0.43± 0.17
NGC884	89	35.553165	57.176613			30.98	−3.29		
NGC884	90	35.563168	57.140194			30.79	−3.21		
NGC884	91	35.567169	57.094028	$1.83^{+1.56}_{-0.47}$	$54.01^{+0.10}_{-0.11}$	31.04	−3.04	2500	0.12± 0.62
NGC884	101	35.605461	57.012085			30.92	−3.20		
NGC884	102	35.611462	57.089748			30.64	−3.87		
NGC884	104	35.614544	57.025196			30.66	−4.33		
NGC884	106	35.626041	57.242638			30.59	−3.41		
NGC884	110	35.643375	57.191418			30.47	−4.65		
NGC884	113	35.655708	57.217945			30.61	−3.35		
NGC884	119	35.707542	57.161026			31.11	−3.42		

Table 5. (*Continued*).

Cluster name	Source detection			kT (keV)	Spectral			Timing	
	ID	RA_{J2000} (deg)	DEC_{J2000} (deg)		log(EM) (cm^{-3})	$\log(L_X)^{\dagger}$ (ergs s^{-1})	$\log(\frac{L_X}{L_{bol}})$	Bin size (s)	F_{var}
NGC884	121	35.722958	57.098804			<30.53	<−4.41		
NGC884	122	35.724209	57.126083	$1.02^{+0.27}_{-0.21}$	$53.88^{+0.12}_{-0.14}$	30.96	−3.78		
NGC884	130	35.747002	57.137417			30.44	−4.08		
NGC884	137	35.803707	57.122444			30.74	−3.42		
NGC884	138	35.820457	57.222500			31.27	−3.29		
NGC7380	34	341.70270	58.133194			30.86	−4.59		
NGC7380	35	341.72348	58.168083			<31.28	<−2.87		
NGC7380	37	341.72653	58.134724			30.88	−3.41		
NGC7380	41	341.74469	58.076694			30.92	−3.16		
NGC7380	46	341.77658	58.113888			31.09	−2.81		
NGC7380	48	341.80121	58.109417	$1.78^{+2.35}_{-0.60}$	$54.06^{+0.16}_{-0.22}$	31.09	−3.30		
NGC7380	49	341.80286	58.191334			31.06	−3.29		
NGC7380	50	341.81659	58.067890	$1.37^{+0.51}_{-0.22}$	$54.18^{+0.13}_{-0.15}$	31.20	−3.20		
NGC7380	57	341.89398	58.138054			31.25	−3.27		
NGC7380	60	341.89981	58.049862			31.08	−2.72		
NGC7380	62	341.90005	58.075222	$2.72^{+3.98}_{-0.92}$	$54.36^{+0.12}_{-0.14}$	31.45	−3.12		
NGC7380	65	341.91592	58.099998			30.96	−3.00		
NGC7380	66	341.91595	58.023472	>4.68	$54.48^{+0.18}_{-0.14}$	31.69	−2.75	1200	0.15±0.53
NGC7380	67	341.92245	58.148861	$1.64^{+1.25}_{-0.46}$	$54.44^{+0.12}_{-0.14}$	31.48(?)	−2.34(?)		
NGC7380	70	341.93970	58.058472			31.13	−2.99		
NGC7380	71	341.94296	58.184776			31.12(?)	−2.49(?)		
NGC7380	80	341.97977	58.056499			31.14	−2.69		
NGC7380	82	342.00183	58.044971			31.03	−3.20		
NGC7380	83	342.01785	58.068554			31.22	−2.85		
NGC7380	85	342.02817	58.075195	$6.50^{+4.31}_{-2.22}$	$55.03^{+0.05}_{-0.05}$	32.22	−2.06		
NGC7380	86	342.12955	58.147583			31.43	−4.00		

Table 5. (*Continued*).

Cluster name	Source detection ID	RA_{J2000} (deg)	DEC_{J2000} (deg)	kT (keV)	Spectral log(EM) (cm^{-3})	log(L_X)† (ergs s^{-1})	log($\frac{L_X}{L_{bol}}$)	Timing Bin size (s)	F_{var}
Berkeley 86	75	305.04169	38.721001	$1.87^{+1.63}_{-0.63}$	$54.15^{+0.10}_{-0.12}$	31.18	−4.24	2500	0.22±0.34
Berkeley 86	81	305.08072	38.700722			30.92(?)	−2.27(?)		
Berkeley 86	84	305.08899	38.687695			<30.78	< −4.51		
Berkeley 86	89	305.10193	38.700638			31.21	−4.50		
Berkeley 86	93	305.12442	38.665749			30.98	−2.75		
IC2602	6	160.24988	−64.334000	$1.31^{+0.31}_{-0.09}$	$52.21^{+0.05}_{-0.06}$	29.24	−3.43	400	1.02±0.09
IC2602	16	160.36188	−64.339302	$2.33^{+4.80}_{-0.74}$	$51.34^{+0.13}_{-0.16}$	27.80	−3.67		
IC2602	20	160.43851	−64.467941	$1.22^{+0.05}_{-0.05}$	$52.64^{+0.03}_{-0.03}$	29.68	−3.18	300	0.19±0.05
IC2602	48	160.67279	−64.351387	$0.94^{+0.01}_{-0.01}$	$53.22^{+0.01}_{-0.01}$	30.29	−3.41	400	0.25±0.02
IC2602	54	160.71042	−64.364891	$0.93^{+0.09}_{-0.20}$	$51.55^{+0.06}_{-0.07}$	28.65	−3.06	1500	0.22±0.16
IC2602	66	160.81512	−64.398415	$0.62^{+0.04}_{-0.04}$	$52.13^{+0.03}_{-0.03}$	29.22	−4.37	800	0.13±0.08
IC2602	67	160.84492	−64.486832	$0.80^{+0.19}_{-0.08}$	$51.88^{+0.05}_{-0.05}$	28.99	−3.21	1000	0.21±0.14
IC2602	87	161.04083	−64.247528	$0.95^{+0.06}_{-0.18}$	$52.12^{+0.05}_{-0.05}$	29.22	−3.39	1000	0.19±0.10
IC2602	90	161.08730	−64.502136	$0.72^{+0.24}_{-0.29}$	$51.70^{+0.12}_{-0.14}$	28.81	−3.08		
IC2602	91	161.09322	−64.258446	$0.73^{+0.07}_{-0.07}$	$52.00^{+0.05}_{-0.05}$	29.11	−4.40	1000	0.28±0.12
Hogg15	10	190.79047	−63.076221			31.03	−3.43		
Hogg15	13	190.80016	−63.146889			31.15	−3.34		
Hogg15	14	190.80179	−63.102390	$0.96^{+0.31}_{-0.27}$	$54.21^{+0.14}_{-0.16}$	31.31	−4.69		
Hogg15	16	190.82042	−63.084251	$0.63^{+0.19}_{-0.40}$	$54.35^{+0.72}_{-0.17}$	31.45	−3.96		
Hogg15	18	190.82851	−63.083611			31.06	−4.98		
Hogg15	21	190.83771	−63.015751	$0.830^{+0.14}_{-0.21}$	$54.44^{+0.13}_{-0.13}$	31.55	−4.18		
Hogg15	24	190.85812	−63.105526			31.56	−2.67		
Hogg15	30	190.89046	−63.065945			31.03	−4.70		
Hogg15	31	190.89145	−63.073444			30.92	−5.40		

Table 5. (*Continued*).

Cluster name	Source detection ID	RA$_{J2000}$ (deg)	DEC$_{J2000}$ (deg)	kT (keV)	Spectral log(EM) (cm^{-3})	log(L_X)† (ergs s^{-1})	log($\frac{L_X}{L_{bol}}$)	Timing Bin size (s)	F_{var}
Hogg15	32	190.89250	−63.001778			30.92	−4.66		
Hogg15	35	190.90747	−63.157776	$0.510^{+0.24}_{-0.21}$	$54.49^{+0.36}_{-0.20}$	31.54	−3.83		
Hogg15	37	190.93520	−63.099888	$2.34^{+0.81}_{-0.49}$	$54.71^{+0.06}_{-0.07}$	31.77	−2.59	1000	0.30±0.15
Hogg15	50	190.98984	−63.164001	$0.640^{+0.19}_{-0.13}$	$54.64^{+0.11}_{-0.13}$	31.73	−4.04		
Hogg15	52	190.99983	−63.008915			30.76	−3.49		
Hogg15	56	191.00992	−63.171501			30.92	−3.41		
Hogg15	70	191.09630	−63.062611			31.42	−4.18		
Hogg15	71	191.09637	−63.123444	$0.860^{+0.21}_{-0.27}$	$54.12^{+0.13}_{-0.16}$	31.33	−4.11		
Hogg15	72	191.10333	−63.099804			30.87	−4.68		
Trumpler 18	79	167.89359	−60.655224	$1.92^{+2.87}_{-0.75}$	$53.36^{+0.10}_{-0.12}$	30.38	−5.26		
Trumpler 18	84	167.90800	−60.666779	>26.50	$53.82^{+0.07}_{-0.11}$	30.92	−2.75		
Trumpler 18	85	167.90945	−60.679501	$12.60^{+30.50}_{-5.97}$	$53.86^{+0.10}_{-0.06}$	31.05	−3.54		

Notes: Column 1: Cluster name; Column 2: identification number (ID) in Supplementary Table 3; Column 3 and 4 represent the position of X-ray source; Column 5, 6, 7: estimated values of coronal temperatures (kT), emission measure (EM) and X-ray luminosities (log(L_X)) from either spectral fitting using C-statistics or derived from conversion of count rates into X-ray fluxes using CCFs†. Column 8: Time bin size in s; Column 9: represent fractional root mean square variability amplitude (F_{var}) with errors and not defined when S^2 is lesser than $\langle\sigma^2_{err}\rangle$ (for details see §4).

†: X-ray flux derived from spectral fitting are converted into luminosities using the distance to their corresponding clusters (see Table 1). The spectral parameters are not derived for the stars with poor count statistics and their unabsorbed X-ray fluxes have been estimated by their count rates in EPIC detector using CCFs (WebPIMMS), i.e., flux = CCF × count rates. The values of CCFs (in units of erg s^{-1} cm^2) are derived for PN and MOS detectors. For Intermediate mass stars: 3.926×10^{-12} and 1.247×10^{-11} for NGC 869 at 2.07 keV; 3.528×10^{-12} and 1.181×10^{-11} for NGC 884 at 1.30 keV; 4.799×10^{-12} and 1.433×10^{-11} for NGC 7380 at 2.38 keV; 1.835×10^{-11} and 6.740×10^{-11} for Hogg 15 at 0.29 keV; For low mass stars: 4.937×10^{-12} and 1.847×10^{-11} for NGC 663 at 0.71 keV; 3.926×10^{-12} and 1.292×10^{-11} for NGC 869 at 2.05 keV; 3.610×10^{-12} and 1.206×10^{-11} for NGC 884 at 1.59 keV; 4.931×10^{-12} and 1.460×10^{-11} for NGC 7380 at 2.80 keV; 6.054×10^{-12} and 1.749×10^{-11} for Berkeley 86 at 1.87 keV; 7.689×10^{-11} and 2.290×10^{-11} for Hogg 15 at 0.97 keV.

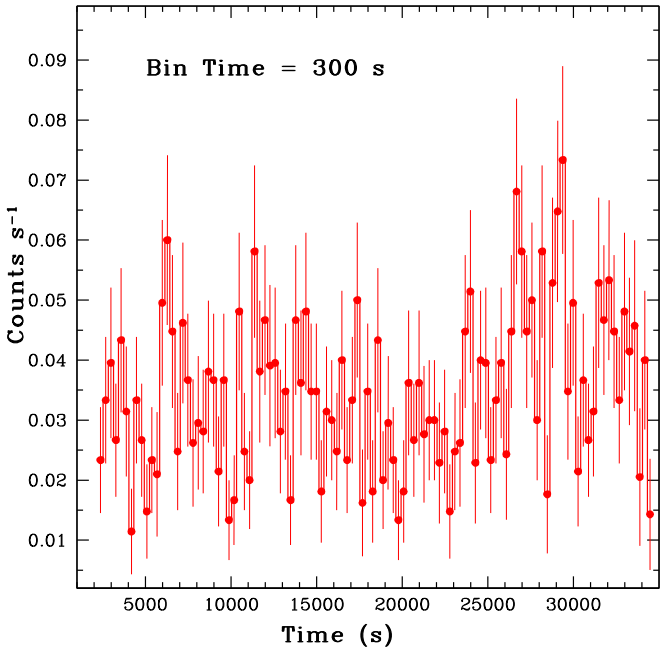

Figure 2. Background subtracted X-ray light curve of the source with ID #20 in the open cluster IC 2602. This source is close to the BY Dra type variable star V554 Car.

The $F_{\rm var}$ is found to be more than 3σ of its error for seven sources (see Table 5), therefore, these sources are considered as variable. The light curves of six sources show characteristics of flares and analyses of these flares are presented in Bhatt *et al.* (2013) (hereafter, Paper II). The background subtracted light curve of one remaining source with ID #20 in the cluster IC 2602 with ID #20 in the cluster IC 2602 is shown in Fig. 2. This source is very close to V554 Car, which is classified as BY-Dra type variable (Kazarovets *et al.* 2001). The X-ray light curve of the source shows $\sim$20% of variability with respect to its mean count rate during observational time scale and does not show any flare-like feature. BY Dra type of star may have rotational modulation in X-rays (see Patel *et al.* 2013).

5. X-ray spectra

Spectral characteristics of stars are also required before one can estimate their luminosity functions. X-ray spectra of the sources with counts greater than 40 have been generated using the SAS task ESPECGET, which also computed the photon redistribution matrix and ancillary matrix. For each source, the background spectrum was obtained from source-free regions chosen according to the source location (same regions as used in the generation of light curves). Spectral analysis was performed based on global fitting using the Astrophysical Plasma Emission Code (APEC) version 1.10 modelled by Smith *et al.* (2001) and implemented in the XSPEC version 12.3.0. The plasma model APEC calculates both line and continuum emissivities for a

hot, optically thin plasma that is in collisional ionization equilibrium. The absorption towards the stars by interstellar medium was accounted for by using a multiplicative model PHABS in XSPEC which assumes the photo-electric absorption cross sections according to Balucińska–Church & McCammon (1992).

The simplest spectral model considered, is that of an isothermal gas which we refer to as the '1T APEC' model. This model is expressed as PHABS × APEC. We adopted the approach used in Currie *et al.* (2009) for X-ray spectral fitting and used an initial temperature kT of 1.5 keV to start the spectral fitting which is a compromise between values typical of stars in younger clusters (e.g., M17; Broos *et al.* 2007) and stars in older clusters (e.g., the Pleiades; Daniel *et al.* 2002). Elemental abundance parameter with a value of 0.3 solar is routinely found in fits of stellar X-ray spectra, and was thus fixed to this value in our analysis (Feigelson *et al.* 2002; Currie *et al.* 2009) for intermediate and low mass stars. For massive stars, however, abundance parameter of 0.2 solar was fixed for fitting (see Bhatt *et al.* 2010; Zhekov & Palla 2007). The value of absorption column density, N_H, was fixed throughout the fitting to the value derived using the relation given by Vuong *et al.* (2003), $N_H = 5 \times 10^{21} \times E(B-V)$ cm^{-2}, and given in Table 1. The temperature, kT and the normalization were the free parameters in spectral fitting. We performed C-statistic model fitting technique rather than using χ^2-minimization technique because of the poor count statistics. The temperature, normalization and unabsorbed flux values were derived by this fitting technique. The estimated temperatures, EM and luminosities are given in Table 6 for the massive stars and in Table 5 for the intermediate and low mass stars. A few examples of X-ray spectra of massive, intermediate and low mass stars are shown in Fig. 3 along with the ratios of the X-ray data to the fitted model in the lower panels.

The X-ray fluxes of the probable cluster members having very poor count statistics (counts below 40) or which were lying between the inter-chip gaps between PN CCDs, were derived from their X-ray count rates in the EPIC detectors estimated from the SAS task EDETECT_CHAIN (see section 2.1 and supplementary material). The CCFs to convert count rates into X-ray fluxes were estimated from WebPIMMS[5] using 1T APEC plasma model. The value of the model parameter N_H was fixed from Table 1 for the respective clusters. However, abundance parameter was fixed at 0.2 solar for massive stars (Zhekov & Palla 2007; Bhatt *et al.* 2010), and 0.3 solar for intermediate and low mass stars (Feigelson *et al.* 2002; Currie *et al.* 2009). The plasma temperature was fixed at 1.0 keV for massive stars (Nazé 2009). However, for intermediate and low mass stars, the plasma temperature was taken as the mean of the temperatures derived from the spectral fitting of other bright stars in the cluster. The mean values of X-ray temperatures of intermediate mass stars have been found to be 2.07, 1.30, 2.38 and 0.29 keV for the open clusters NGC 869, NGC 884, NGC 7380 and Hogg 15, respectively. In the case of low mass stars, the mean values of X-ray temperatures have been found to be 0.71, 2.05, 1.59, 2.80, 1.87, 1.06 and 0.97 keV for the open clusters NGC 663, NGC 869, NGC 884, NGC 7380, Berkeley 86, IC 2602 and Hogg 15, respectively. The derived values of conversion factors of count rates into unabsorbed fluxes for massive, intermediate and low mass stars have been

[5] http://heasarc.gsfc.nasa.gov/cgi-bin/Tools/w3pimms/pim_adv

Table 6. X-ray temperatures and luminosities of massive stars within young clusters.

Cluster	ID	Name	Spectral type	B[a]	Off[b] ($''$)	$kT_{\rm av}$ (keV)	$\log(L_{\rm X})$ (References) (erg s^{-1})	$\log(\frac{L_{\rm X}}{L_{\rm bol}})$
NGC663	26	BD+60 329	B1V		2.3		31.16 (Nazé 2009)	−6.69
NGC663	69	V831 Cas	B1V	Y	1.1	$1.11^{+0.07}_{-0.06}$	34.15 (La Palombara & Mereghetti 2006)	–
NGC869	12	HD 13969	B0.5I		1.8		30.53[††] (Present study)	−7.37
NGC869	50	HD 14052	B1.5I		4.3	$0.44^{+0.18}_{-0.11}$	31.06 (Present study)	−7.34
NGC869	103	[SHM2002] 120	B1.5V		6.3		30.84[††] (Present study)	−7.18
NGC869	109	BD+56 527	B2I		2.0	$1.12^{+0.37}_{-0.21}$	31.02 (Present study)	−7.33
NGC869	119	[SHM2002] 138	B		5.6	$4.64^{+21.04}_{-2.5}$	31.09 (Present study)	−6.43
NGC884	79	[SHM2002] 131	B1.5III		4.4		30.80 (Nazé 2009)	−6.76
NGC884	93	BD+56 578	B2III		2.2		30.89 (Nazé 2009)	−7.14
NGC7380	36	DH Cep	O5.5V+O6.5V	Y	0.6	$0.64^{+0.02}_{-0.02}$	32.43 (Bhatt *et al.* 2010)	−6.71
NGC7380	77	LS III +57 90	O8V((f))	Y	1.7		31.55 (Nazé 2009)	−6.66
Be86	85	HD 228989	O9V+O9V	Y	2.7	$0.62^{+0.15}_{-0.11}$	31.72 (Present study)	−6.62
Hogg15	3	HD 110432	B0.5Vep	Y	2.2	8.0 –11.0	35.00 (Lopes de Oliveira *et al.* 2007)	–
Hogg15	49	MO 1- 78	OB		1.9	$0.72^{+0.23}_{-0.17}$	31.39 (Present study)	−6.91
Hogg15	69				2.1		30.94[††] (Present study)	−6.72
Hogg15	73				0.4		30.94[††] (Present study)	−7.02

[a] 'Y' represents the binarity of stars from literature.

[b] Offset between the position of massive stars in 2MASS catalogue and their X-ray counterparts.

[††] $L_{\rm X}$ has been derived from the X-ray flux estimated from the count rate conversion in PN detector using the WebPIMMS, i.e., flux = CCF × count rate. The values of CCFs (in units of erg s^{-1} cm^2) have been derived for massive stars in PN are 3.606×10^{-12} for NGC 869 and 7.689×10^{-12} for Hogg 15, respectively.

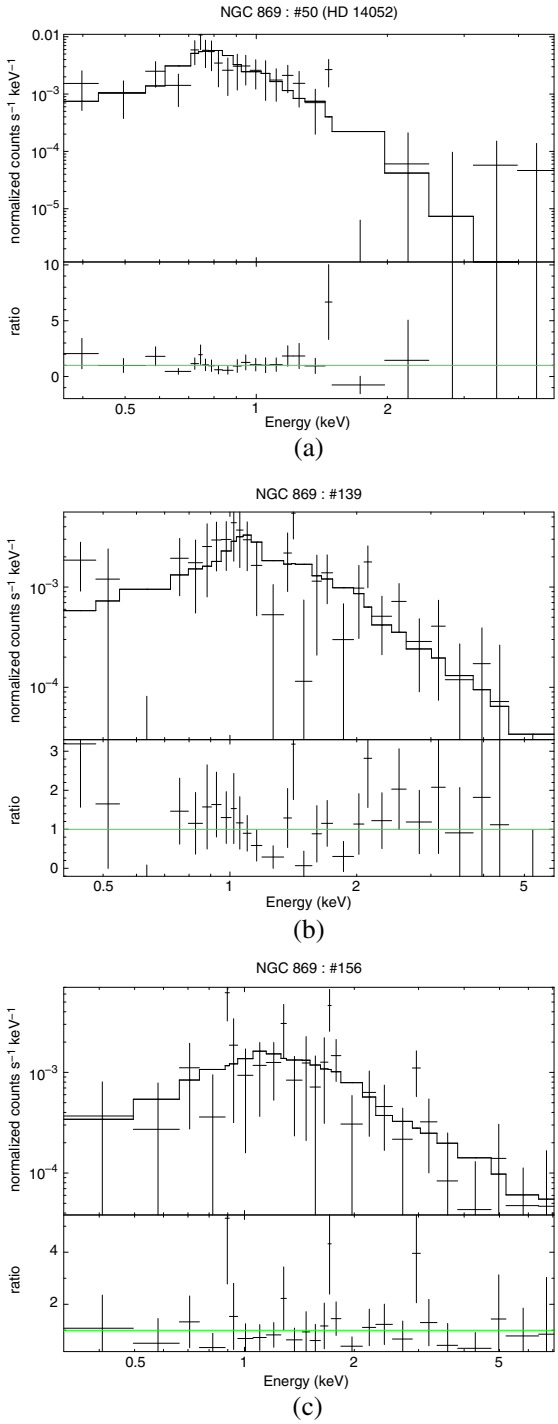

Figure 3. A few example of X-ray spectra of (**a**) massive star, (**b**) intermediate mass star and (**c**) low mass star. The ID of the star with the information of its respective cluster is given at the top of each panel.

given in the footnotes of Tables 5 and 6. For the sources either falling in between the inter-chip gaps of PN CCDs or outside the PN coverage area, the X-ray fluxes in the MOS1 and the MOS2 detectors were estimated from their count rates using CCFs in the MOS detector. The average value of X-ray flux in the MOS1 and MOS2 detectors has been quoted in Table 5. Thus, the X-ray luminosities were estimated from the derived values of the X-ray fluxes and given in Table 6 for massive stars and in Table 5 for intermediate and low mass stars.

X-ray spectrum of star #79 in Berkeley 86 could not be fitted with the model used for spectral fitting, therefore, the N_H parameter was varied as a free parameter. The best-fit value of N_H has been found to be 3×10^{22} cm^{-2}, which is 8 times higher than that expected in the direction of the open cluster Berkeley 86 (see Table 1). This points to either very high intrinsic extinction in the source or the source does not belong to the open cluster Berkeley 86. For the stars showing flares, the values of parameters listed in Table 5, were derived from the spectral fitting performed for their quiescent state data.

6. X-ray properties of stars in different mass groups

X-ray spectral properties of massive, intermediate and low mass stars were analysed separately, because the production mechanism of X-rays are different for different types of stars. The bolometric luminosities ($L_{\rm bol}$) of the stars were derived from their bolometric magnitudes ($m_{\rm bol}$). The absolute J_0 magnitudes were estimated from their observed 2MASS J magnitudes using well constrained age, reddening and distance parameters of the corresponding open clusters in literature (see Table 1). The $m_{\rm bol}$ of the stars were derived from their J_0 magnitudes by interpolating the $m_{\rm bol}$ between J_0 magnitude points in theoretical isochrones of Girardi *et al.* (2002) for MS stars and Siess *et al.* (2000) for PMS stars, depending upon the age of the open cluster.

6.1 *Massive stars*

Our sample contains 16 massive stars of which 6 were reported previously (see references in Table 6). The best fit spectral parameters for 8 stars are given in Table 6. The X-ray fluxes for four massive stars (see Table 6) were derived from their count rates in PN detector by using CCFs. The X-ray temperatures are found to be less than 1.2 keV in general. However, X-ray temperatures are found to be higher in the case of high mass X-ray binary HD 110432 (Lopes de Oliveira *et al.* 2007) and [SHM202] 138. The $L_{\rm X}$ of massive stars lie in the range of 10^{31-35} erg s^{-1}. The $L_{\rm X}/L_{\rm bol}$ for each massive star is derived and given in Table 6. The average value of $\log(L_{\rm X}/L_{\rm bol})$ is found to be -6.92 with standard deviation of 0.31. This value of $L_{\rm X}/L_{\rm bol}$ is broadly consistent with the value derived for a sample of nearly 300 massive stars by Náze (2009).

6.2 *Low mass stars*

Although, there is strong evidence that X-ray emission originates from magnetically confined coronal plasma in the PMS low mass stars (e.g., Preibisch *et al.* 2005), the

relationship between rotation and X-ray activity in PMS low mass stars remained unclear. During the PMS phase, the low mass stars undergo substantial changes in their internal structure, evolving from fully convective structure to a radiative core plus convective envelope structure. Consequently, the stellar properties of low mass stars—$L_{\rm bol}$, magnetic activity and rotation etc., are also changing during the PMS phase. The dependence of $L_{\rm bol}$ and age upon X-ray emission is examined in the following sections.

6.2.1 *X-ray temperatures.* Most of these sources have plasma temperatures between 0.2 and 3 keV which are consistent with values derived for PMS stars in young clusters e.g., NGC 1333 (Getman *et al.* 2002), Orion (Feigelson *et al.* 2002), NGC 1893 (Caramazza *et al.* 2012) and M16 (Guarcello *et al.* 2012). The average plasma temperature of the stars in the open clusters appears to be constant for all stars undergoing PMS evolution from 4 Myr to 46 Myr, and the median value is found to be $\sim$1.3 keV.

6.2.2 *X-ray luminosity functions and their evolution with age.* X-ray Luminosity Functions (XLFs) of low mass stars in different clusters have been derived using Kaplan Meier (KM) estimator of integral distribution functions and shown in Fig. 4(a). No significant difference is observed in the XLFs of low mass stars with ages in the range of 4 to 14 Myr. However the XLF of low mass stars in the open cluster IC 2602 with an age of 46 Myr appears to be lower than that of others. The mean values of log $L_{\rm X}$ with their standard deviations have been found to be 31.26 ± 0.38, 30.82 ± 0.31, 30.81 ± 0.26, 31.22 ± 0.31, 31.01 ± 0.18, 29.10 ± 0.65, 31.24 ± 0.32 and 30.78 ± 0.35 erg s^{-1} for the open clusters NGC 663, NGC 869, NGC 884, NGC 7380, Berkeley 86, IC 2602, Hogg 15 and Trumpler 18, respectively. The mean values of $L_{\rm X}$ of low mass PMS stars are thus nearly similar in all the open clusters except IC 2602.

The evolution of the mean value of log $L_{\rm X}$ with age is shown in Fig. 4(b). The majority of the low mass stars in our sample have masses greater than $1.4 M_{\odot}$ as seen in Fig. 1, except for the stars in IC 2602. The stars in the open cluster IC 2602 with masses above $1.4 M_{\odot}$ may have $L_{\rm X}$ below 27.57 erg s^{-1} (detection limits) and are not detected in the present study. It indicates a sudden decrease in the $L_{\rm X}$ between 14 to 46 Myr for the stars with masses above $1.4 M_{\odot}$. Thus $L_{\rm X}$ is nearly constant during the evolution of low mass stars in PMS phase from 4 to 14 Myr and may decrease thereafter. Scholz *et al.* (2007) reported that the rotation rates increase in the first few Myr of their evolution. It is, therefore, possible that an increase in the X-ray surface flux due to an increase in the rotation rate may be compensated by a decrease in the stellar surface area during PMS evolution, between 1 to 10 Myr, as described by Preibisch (1997). Between 10 to 40 Myr, the decrease in $L_{\rm X}$ may be linked with a rapid spin down in the stars, as suggested by Bouvier *et al.* (1997). However, the faintest cluster members have not been detected here, therefore, the complete XLFs of these clusters cannot be derived since the mean luminosities of the entire cluster population may be lower than these values. Further, in case of low mass close binaries the hot winds produced by the coronae in young stars may drive the evolution of X-rays (Iben and Tutukov 1984).

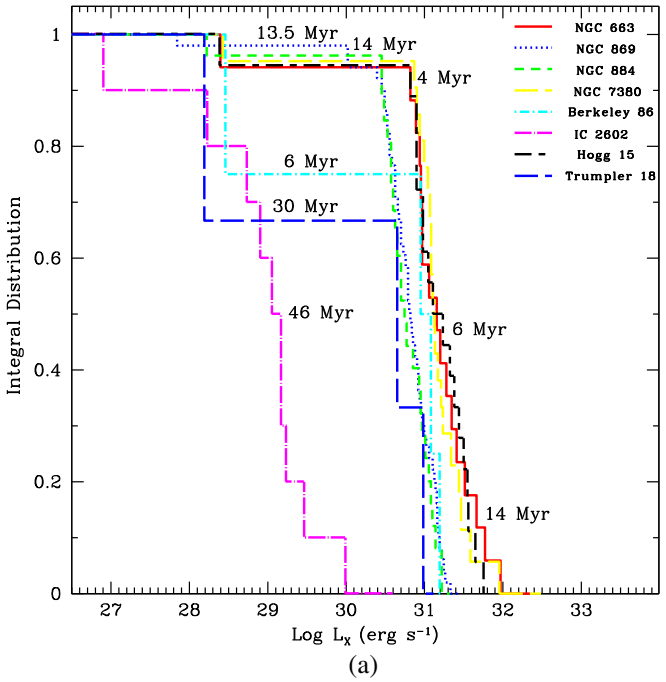

(a)

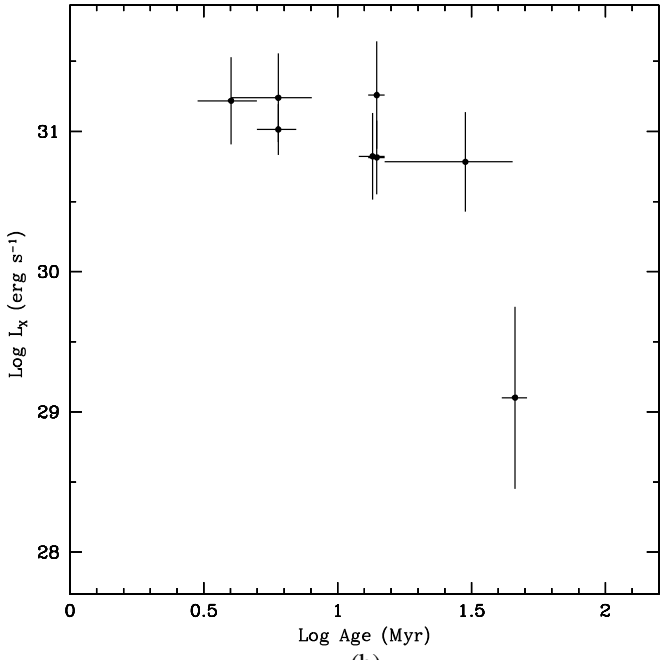

(b)

Figure 4. X-ray luminosities of low mass stars. (**a**) XLFs of low mass stars in different clusters. (**b**) Evolution of mean L_X of the clusters with age.

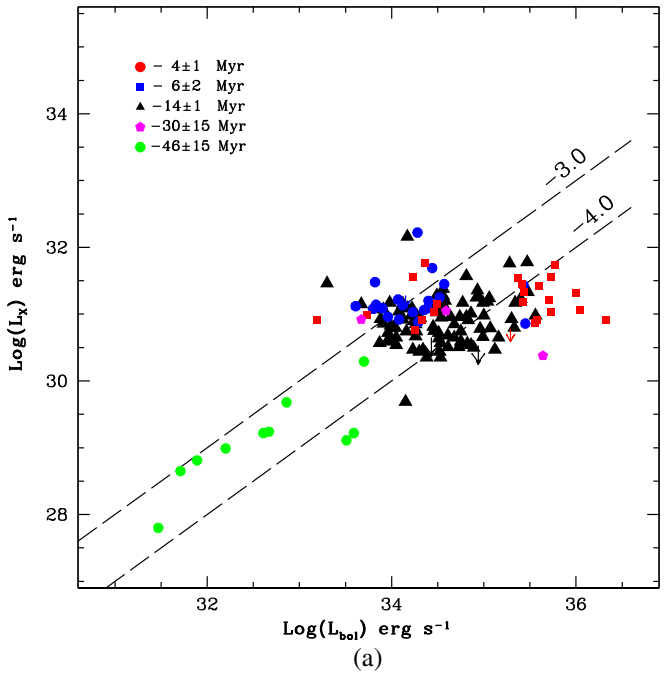

(a)

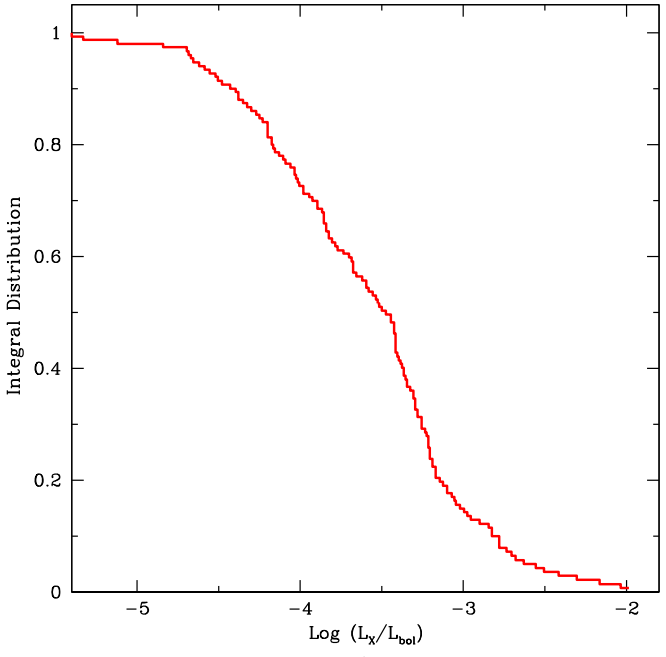

(b)

Figure 5. (**a**) Relation between $L_{\rm X}$ and $L_{\rm bol}$ for low mass stars in the sample. Dashed lines in each plot represent the isopleths of $\log(L_{\rm X}/L_{\rm bol})$ and the values are given above each line. (**b**) Distribution of $\log L_{\rm X}/L_{\rm bol}$ ratio for all the low mass stars in all the clusters.

6.2.3 *X-ray to bolometric luminosity ratios.* L_X/L_{bol} provides an estimate of the fraction of total stellar energy that is dissipated through coronal heating, and the estimated values of the L_X/L_{bol} for low mass stars in our sample are listed in Table 5. The mean values of $\log(L_X/L_{bol})$ with standard deviations are found to be -3.86 ± 0.41, -3.63 ± 0.49, -3.63 ± 0.51, -3.12 ± 0.53, -4.00 ± 0.84, -3.52 ± 0.49, -4.02 ± 0.78 and -3.85 ± 1.28 for the open clusters NGC 663, NGC 869, NGC 884, NGC 7380, Berkeley 86, IC 2602, Hogg 15 and Trumpler 18, respectively. These values have been found to be consistent with the values derived for the young clusters: the Orion (-3.39 ± 0.63), IC 348 (-3.53 ± 0.43) and NGC 2547 (-3.20 ± 0.24) (see Alexander & Preibisch 2012). The derived values of mean $\log(L_X/L_{bol})$ for each cluster are similar and the mean value $\log(L_X/L_{bol})$ is found to be -3.6 with a standard deviation of 0.4 for the collective sample of low mass stars within these open clusters.

The relation between L_X and L_{bol} along with the isopleths of $\log(L_X/L_{bol}) = -3.0$, -4.0 are shown in Fig. 5(a). It can be seen that most of the sources have L_X/L_{bol} values below the saturation level. The distribution of $\log(L_X/L_{bol})$ for all the low mass stars in all the clusters has been shown in Fig. 5(b) which is derived using the KM estimator of integral distribution functions. It shows that only 15% of the X-ray sources have L_X/L_{bol} values above the saturation level. There are five sources with $\log(L_X/L_{bol})$ greater than -2.5; values that are very unlikely to be

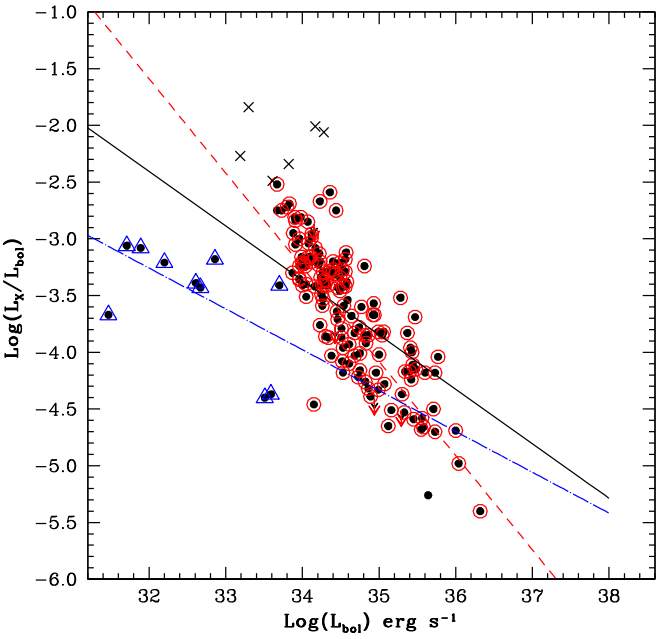

Figure 6. Relation between (L_X/L_{bol}) and L_{bol} for low mass stars in the sample (dots), for stars with age from 4 to 14 Myr (open circles), and for the stars in the cluster IC 2602 with age of 46 Myr (open triangles) derived using least square fitting and shown by continuous line, dashed line and dashed plus dotted line, respectively. The stars with $\log(L_X/L_{bol})$ above -2.5 have not been considered while deriving these relations and are marked by the symbol of cross.

found for stellar sources. This is possibly the result of these sources not being members of the corresponding clusters, therefore, their L_X and L_{bol} may have not been estimated properly. The L_X values of these few sources are marked with a symbol of question mark in Table 5. These sources are marked with the symbol of cross in Fig. 6, and were not considered for further analysis. The evolution of $\log(L_X/L_{bol})$ with age is shown in Fig. 7 and found that the $\log(L_X/L_{bol})$ is nearly constant during 4 to 46 Myr.

Among the low mass PMS stars in the Orion, the median L_X/L_{bol} is 2–3 orders of magnitude greater, i.e., $\approx 10^{-3}$, than that found within ZAMS stars and therefore their fractional X-ray luminosities are 'saturated'. Currie *et al.* (2009) showed that the stars with masses $>1.5 M_\odot$ deviate from X-ray saturation by ≈10–15 Myr. The present analysis indicates that most of the low mass PMS stars come out from the saturation limit earlier than 4–8 Myr, which is quite early as compared to the age described by Currie *et al.* (2009), i.e., 10–15 Myr. The X-ray emission depends upon the magnetic dynamo that is the result of a combination of turbulent convection and rotation within the convection zone. As a low mass star contracts onto the MS, its internal structure changes and its outer convective zones shrinks. Therefore, the evolution of fractional X-ray luminosity with age might be due to either the change in the internal structure of a star or spin-down rotation of a star during the PMS phase, or both. Alexander & Preibisch (2012) showed that there was no correlation between the L_X/L_{bol} and the rotation period. They also found some rather slowly rotating stars (period > 10 days) with very strong X-ray activity, and suggested that instead of rotation it is the change in the internal structure of PMS stars during the

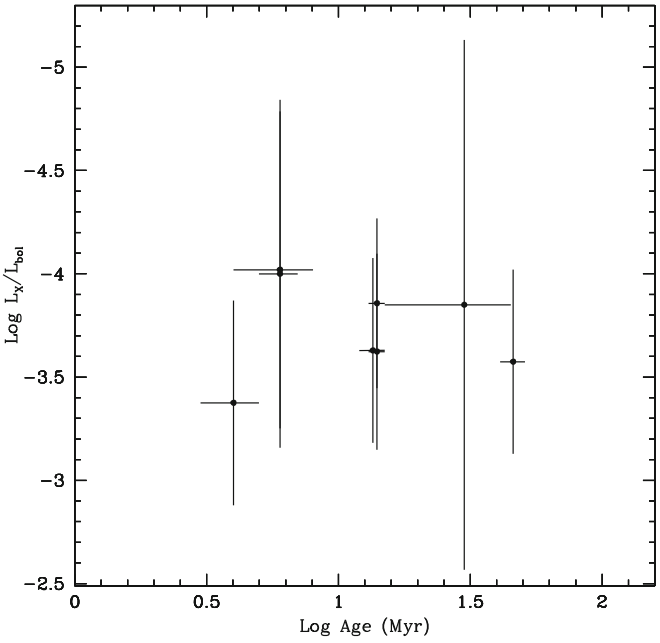

Figure 7. Evolution of mean L_X/L_{bol} of the clusters with age.

evolution which is likely to be responsible for the generation of magnetic dynamo and consequently the X-ray emission.

The dependence of L_X/L_{bol} on L_{bol} is shown in Fig. 6. The correlation coefficients between L_X/L_{bol} and L_{bol} have been derived using Pearson product-moment test and Kendall tau rank test, and their values are found to be -0.65 and -0.58, respectively for all the low mass stars in the sample. Thus, the probability of no correlation between L_X/L_{bol} and L_{bol}, i.e., the null hypothesis, is estimated to be 2.2×10^{-16} from both the tests.

The linear regressions have been calculated using the least-squares Marquardt–Levenberg algorithm (Press *et al.* 1992) corresponding to the following relation for all the low mass stars and shown by continuous line in Fig. 6,

$$\log(L_X/L_{bol}) = -0.48(\pm 0.05) \times \log(L_{bol}) + 12.95(\pm 1.63). \quad (3)$$

For the low mass stars with ages between 4 to 14 Myr and shown by dashed line in Fig. 6,

$$\log(L_X/L_{bol}) = -0.83(\pm 0.05) \times \log(L_{bol}) + 24.97(\pm 1.70). \quad (4)$$

For the low mass stars in the open cluster IC 2602 with ages 46 Myr and shown by dashed and dotted line in Fig. 6,

$$\log(L_X/L_{bol}) = -0.36(\pm 0.17) \times \log(L_{bol}) + 8.26(\pm 5.69). \quad (5)$$

Equation (3) shows a power-law dependence of the fractional X-ray luminosity on L_{bol} during 4 to 46 Myr. The power-law indices are found to be different for stars with age of 4–14 Myr and the stars in the cluster IC 2602 with age ∼46 Myr from eq. (4) and eq. (5), respectively. Prebisch *et al.* (2005) showed $L_X \propto L_{bol}$ for the stars in Orion which implies that L_X/L_{bol} is nearly constant at 1 Myr. For NEXXUS sample of nearby field stars (Schmitt & Liefke 2004), Prebisch *et al.* (2005) found $L_X \propto L_{bol}^{0.42}$, which implies that $(L_X/L_{bol}) \propto L_{bol}^{-0.58}$. The values of power-law indices of L_X and L_X/L_{bol} relation for the open clusters NGC 663, NGC 869, NGC 884, NGC 7380, Berkeley 86, IC 2602 and Hogg 15 are derived to be -0.7 ± 0.2, -0.8 ± 0.1, -1.1 ± 0.1, -1.0 ± 0.1, -0.9 ± 0.1, -0.4 ± 0.2, -1.0 ± 0.1, respectively. It implies that the (L_X/L_{bol}) depends upon L_{bol} during 4 to 46 Myr and this dependence upon L_{bol} may be started earlier than 4 Myr. As low mass stars evolve to MS, their effective temperatures eventually increase and the depth of their convective envelopes reduce, therefore their L_{bol} changes. During 4 Myr to 46 Myr, the L_{bol} increases nearly three times (Siess *et al.* 2000) for low mass star with masses in the range of 1.4–2.0$M_\odot$. This increase in L_{bol} can produce a decrease of nearly one-third in (L_X/L_{bol}) which can give a decrease of nearly 0.5 dex in logarithmic scale. Such a variation cannot be distinguished using present data because the standard deviation in $\log(L_X/L_{bol})$ is comparable with the decrease of 0.5 dex.

6.3 *Intermediate mass stars*

A convincing and unique explanation for the generation of X-ray emission from intermediate mass stars has not been forthcoming, despite abundant speculations about the possible mechanisms. The presence of magnetic field of the order of a few hundred Gauss (Donati *et al.* 1997; Hubrig *et al.* 2004; Wade *et al.* 2005) has been

detected in these stars, that can support a shear dynamo which may be responsible for X-ray emission from intermediate mass stars as in the T-Tauri stars. At the same time, the option of unresolved companions is also considered because the intermediate mass stars are more likely to be found in binaries, i.e., companion hypothesis (Baines *et al.* 2006; Stelzer *et al.* 2006 and references therein).

The detection limits are in the range of $10^{27.6}$–$10^{30.8}$ erg s^{-1} for different clusters as they are located at different distances from the Earth. For making a sample of intermediate mass stars from different clusters, a highest detection limit of log $L_X \approx 10^{30.8}$ erg s^{-1} among all clusters (see also Table 4) was used, which shows that a star with log $L_X > 30.8$ erg s^{-1} could be detected in any of the clusters. In this way, a total of 27 intermediate-mass stars were identified and examined further. The XLFs of the low mass and intermediate mass stars having log $L_X > 30.8$ erg s^{-1} were derived using the KM estimator of integral distribution functions. A comparison of the X-ray luminosities and fractional X-ray luminosities of low mass stars and intermediate mass stars in the present sample is shown in Fig. 8. The results of two sample tests are given in Table 7. The results of the Wilcoxon Rank Sum, Logrank, Peto and Peto Generalized Wilcoxon and Kolmogorov–Smirnov (KS) statistical tests show that the X-ray luminosity distribution of intermediate mass stars is different from that of low mass stars with confidence of 93%, 98%, 92% and 77%, respectively. Therefore, the X-ray luminosities of both types of stars above this limit of log $L_X(>30.8)$ erg s^{-1} are not significantly different from each other. Further, the

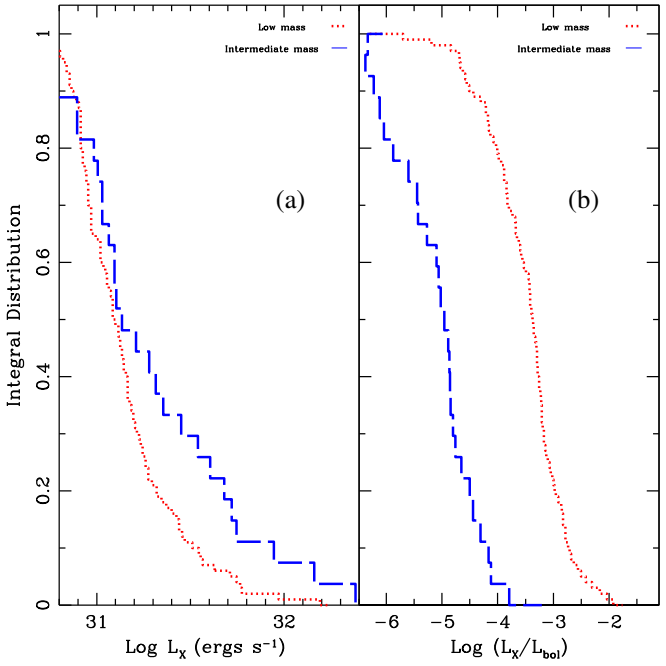

Figure 8. Comparison of the X-ray activity of low mass and intermediate mass stars having log $L_X > 30.8$ erg s^{-1} based on the Kaplan Meier estimator. (**a**) Distribution of L_X and (**b**) distribution of L_X/L_{bol} ratio.

Table 7. Results of two sample tests.

Statistics of objects in two groups	
$\log(L_X)$ (erg s^{-1})	> 30.8
Number of stars (low mass)	100
Number of stars (intermediate mass)	27
Probability of having a common parent L_X distribution	
Wilcoxon rank sum test	0.07
Logrank test	0.02
Peto and Peto generalized Wilcoxon test	0.08
Kolmogorov–Smirnov test	0.23
$\log(L_X/L_{bol})$	
Probability of having a common parent L_X/L_{bol} distribution	
Wilcoxon rank sum test	8.1×10^{-13}
Logrank test	0.0
Peto and Peto generalized Wilcoxon test	0.0
Kolmogorov–Smirnov test	9.6×10^{-12}

L_X/L_{bol} ratio of intermediate mass stars and low mass stars are different, with a confidence of greater than 99.999% using these statistical tests.

Recently, Balona (2013) suggested the light variation due to rotation modulation caused by star-spots in nearly 875 A-type stars using Kepler's data. If A-type stars have spots, then it is natural to expect a magnetic field, and therefore X-ray activity in intermediate mass stars. The median values of $\log(L_X/L_{bol})$ are found to be -5.06 and -3.41 for intermediate mass stars and low mass stars, respectively. It implies that if the intermediate mass stars themselves produce X-rays, the strength of the X-ray activity is possibly weaker as compared to the low mass stars. However, the possibility of the X-ray emission from a nearby low mass star cannot be ruled out here due to the poor spatial resolution data of XMM-Newton.

7. Summary and conclusions

We have described the X-ray source contents of eight young open clusters using the XMM-Newton data. These clusters have ages ranging from 4 Myr to 46 Myr and thus provide a link between the X-ray properties of young clusters like the Orion and older clusters like the Pleiades. The association and membership of these X-ray sources with stars has been deduced using optical and NIR data. Overall 152 X-ray sources have been identified with low mass PMS stars, 36 with intermediate mass stars and 16 with massive stars. The main results are summarized below:

(1) The X-ray temperatures, luminosities and fractional X-ray luminosities of massive stars are consistent with the values reported previously in the literature for other massive stars.
(2) The plasma temperatures are found to be in the range of 0.2 keV to 3 keV with a median value of 1.3 keV for all low mass stars irrespective of their ages.

(3) The observed XLFs of low mass stars in the open clusters with ages from 4 to 14 Myr appear to be similar, which implies that L_X is nearly constant during PMS evolution from 4 to 14 Myr. Therefore, the decrease in L_X of low mass stars may occur during 14 to 100 Myr. Non-detection of X-rays from the stars above $1.4M_\odot$ in the open cluster IC 2602 may give an indication of a sudden decrease in their L_X during 14 to 46 Myr.
(4) The $\log(L_X/L_{bol})$ of most of the low mass stars are below the saturation limits and the mean value has been found to be -3.6 with a standard deviation of 0.4. This value is consistent with the values derived for other young clusters the Orion, IC 348 and NGC 2547. Thus, a deviation of low mass stars with masses greater than $1.4M_\odot$ from X-ray saturation may occur before the age of 4–8 Myr, earlier than the age derived by Currie *et al.* (2009), i.e., 10–15 Myr.
(5) The (L_X/L_{bol}) of low mass stars correlate well with their L_{bol}, suggesting its dependence on the internal structure of stars.
(6) No statistically significant difference in L_X from the intermediate mass and the low mass PMS stars has been detected. But the observed L_X/L_{bol} for intermediate mass stars have been found to be significantly lower than that of low mass stars. It possibly indicates that the strength of X-ray activity in intermediate mass stars is weaker than in the low mass stars. Another possibility is that the origin of X-ray emission from intermediate mass stars might be the result of X-ray emission coming from an unresolved nearby low mass PMS star. Deeper and higher spatial resolution data with CHANDRA is needed to check for this possibility and to estimate the complete XLFs of these clusters.

Acknowledgements

The authors would like to thank the anonymous referee for his/her constructive comments. This publication makes use of data from the Two-Micron All-Sky Survey, which is a joint project of the University of Massachusetts and the Infrared Processing and Analysis Center/California Institute of Technology, funded by the National Aeronautics and Space Administration and the National Science Foundation, and data products from XMM-Newton archives using the high energy astrophysics science archive research center which is established at Goddard by NASA. We acknowledge XMM-Newton Help Desk for their remarkable support in X-ray data analysis. Data from Simbad, VizieR catalogue access tool, CDS, Strasbourg, France have also been used. HB is thankful for the financial support for this work through the INSPIRE Faculty Fellowship granted by the Department of Science & Technology India. They also acknowledge R. C. Rannot, Nilesh Chouhan and R. Koul for their support to complete this work.

References

Alexander, F., Preibisch, T. 2012, *A&A*, **539**, A64.
Baines, D., Oudmaijer, R. D., Porter, J. M., Pozzo, M. 2006, *MNRAS*, **367**, 737.
Balona, L. A. 2013, *MNRAS*, **431**, 2240.
Balucińska-Church, M., McCammon, D. 1992, *ApJ*, **400**, 699.

Bhatt, H., Pandey, J. C., Kumar, B., Sagar, R., Singh, K. P. 2010, *New Astronomy*, **15**, 755.
Bhatt, H., Pandey, J. C., Singh, K. P., Sagar, Ram, Kumar, B. 2013, submitted to JAA.
Bhavya, B., Mathew, B., Subramaniam, A. 2007, *BASI*, **35**, 383.
Bouvier, J., Wichmann, R., Grankin, K., Allain, S., Covino, E., Fernández, M., Martin, E. L., Terranegra, L., Catalano, S., Marilli, E. 1997, *A&A*, **318**, 495.
Brandt, W. N., Hasinger, G. 2005, *ARA&A*, **43**, 827.
Broos, P. S., Feigelson, E. D., Townsley, L. K., Getman, K. V., Wang, J., Garmire, G. P., Jiang, Z., Tsuboi, Y. 2007, *ApJS*, **169**, 353.
Caillault, J.-P., Helfand, D. J. 1985, *ApJ*, **289**, 279.
Caramazza, M., Micela, G., Prisinzano, L., Sciortino, S., Damiani, F., Favata, F., Stauffer, J. R., Vallenari, A., Wolk, S. J. 2012, *A&A*, **539**, 74.
Chen, W. P., Pandey, A. K., Sharma Saurabh, Chen, C. W., Chen, Li, Sperauskas, J., Ogura, K., Chuang, R. J., Boyle, R. P. 2011, *AJ*, **142**, 71.
Crowther, P. A. 2007, *A&AR*, **45**, 177.
Currie, T., Evans, N. R., Spitzbart, B. D., Irwin, J., Wolk, S. J., Hernandez, J., Kenyon, S. J., Pasachoff, J. M. 2009, *AJ*, **137**, 3210.
Currie, T., Hernandez, J., Irwin, J., Kenyon, S. J., Tokarz, S., Balog, Z., Bragg, A., Berlind, P., Calkins, M. 2010, *ApJS*, **186**, 191.
Cutri, R. M., Skrutskie, M. F., van Dyk, S., Beichman, C. A., Carpenter, J. M., Chester, T., Cambresy, L., Evans, T. *et al.* 2003, The IRSA 2MASS All-Sky Point Source Catalog, NASA/IPAC Infrared Science Archive http://irsa.ipac.caltech.edu/applications/Gator/.
D'Orazi, V., Randich, S. 2009, *A&A*, **501**, 553.
Daniel, K. J., Linsky, J. L., Gagné, M. 2002, *ApJ*, **578**, 486.
Delgado, A. J., Alfaro, E. J., Yun, J. L. 2007, *A&A*, **467**, 1397.
Delgado, A. J., Alfaro, E. J., Yun, J. L. 2011, *A&A*, **531**, 141.
Dias, W. S., Alessi, B. S., Moitinho, A., Lépine, J. R. D. 2002, *A&A*, **389**, 871.
Dobbie, P. D., Lodieu, N., Sharp, R. G. 2010, *MNRAS*, **409**, 1002.
Donati, J.-F., Semel, M., Carter, B. D., Rees, D. E., Collier Cameron, A. 1997, *MNRAS*, **291**, 658.
Edelson, R., Krolik, J., Pike, G. 1990, *ApJ*, **359**, 86.
Edelson, R., Turner, T. J., Pounds, K., Vaughan, S., Markowitz, A., Marshall, H., Dobbie, P., Warwick, R. 2002, *ApJ*, **568**, 610.
Fabricius, C., Høg, E., Makarov, V. V., Mason, B. D., Wycoff, G. L., Urban, S. E. 2002, *A&A*, **384**, 180.
Feigelson, E. D., Broos, P., Gaffney, J. A. III, Garmire, G., Hillenbrand, L. A., Pravdo, S. H., Townsley, L., Tsuboi, Y. 2002, *ApJ*, **574**, 258.
Feigelson, E. D., Gaffney, J. A. III, Garmire, G., Hillenbrand, L. A., Townsley, L. 2003, *ApJ*, **584**, 911.
Feigelson, E. D. *et al.* 2004, *ApJ*, **611**, 1107.
Flaccomio, E., Damiani, F., Micela, G., Sciortino, S., Harnden, F. R. Jr., Murray, S. S., Wolk, S. J. 2003a, *ApJ*, **582**, 398.
Flaccomio, E., Micela, G., Sciortino, S. 2003b, *A&A*, **402**, 277.
Flesch, E. 2010, *PASA*, **27**, 283.
Getman, K. V., Feigelson, E. D., Townsley, L., Bally, J., Lada, C. J., Reipurth, B. 2002, *ApJ*, **575**, 354.
Girardi, L., Bertelli, G., Bressan, A., Chiosi, C., Groenewegen, M. A. T., Marigo, P., Salasnich, B., Weiss, A. 2002, *A&A*, **391**, 195.
Glebocki, R., Gnacinski, P. 2005, Catalog of Stellar Rotational Velocities, 3244.
Guarcello, M. G., Caramazza, M., Micela, G., Sciortino, S., Drake, J. J., Prisinzano, L. 2012, *ApJ*, **753**, 117.
Güdel M. 2004, *A&A Rev.*, **12**, 71.
Hubrig, S., Schöller, M., Yudin, R. V. 2004, *A&A*, **428**, 1.

Iben, I. Jr., Tutukov, A. V. 1984, *ApJ*, **284**, 719.
Ikeda, H. *et al.* 2008, *AJ*, **135**, 2323.
Jeffries, R. D., Evans, P. A., Pye, J. P., Briggs, K. R. 2006, *MNRAS*, **367**, 781.
Joshi, H., Kumar, B., Singh, K. P., Sagar, R., Sharma, S., Pandey, J. C. 2008, *MNRAS*, **391**, 1279.
Kazarovets, E. V., Samus, N. N., Durlevich, O. V. 2001, *Information Bulletin on Variable Stars*, **5135**, 1.
Kharchenko, N. V., Roeser, S. 2009, 1280, Available at VizieR On-line Data Catalog http://webviz.u-strasbg.fr/viz-bin/VizieR.
Kudritzki, R. P., Puls, J. 2000, *ARA&A*, **38**, 613.
La Palombara, N., Mereghetti, S. 2006, *A&A*, **455**, 283.
Lopes de Oliveira, R., Motch, C., Smith, M. A., Negueruela, I., Torrejón, J. M. 2007, *A&A*, **474**, 983.
Lucy, L. B., White, R. L. 1980, *ApJ*, **241**, 300.
Micela, G., Sciortino, S., Favata, F., Pallavicini, R., Pye, J. 1999, *A&A*, **344**, 83.
Micela, G., Sciortino, S., Serio, S. *et al.* 1985, *ApJ*, **292**, 172.
Micela, G., Sciortino, S., Vaiana, G. S. *et al.* 1988, *ApJ*, **325**, 798.
Micela, G., Sciortino, S., Vaiana, G. S. *et al.* 1990, *ApJ*, **348**, 557; Solar flares: A monograph from Skylab Solar Workshop II (A80-37026 15-92), 341–409.
Nazé, Y. 2009, *A&A*, **506**, 1055.
Ogura, K., Sugitani, K., Pickles, A. 2002, *AJ*, **123**, 2597.
Owocki, S. P., Cohen, D. H. 1999, *ApJ*, **520**, 833.
Pandey, A. K., Upadhyay, K., Ogura, K., Sagar, R., Mohan, V., Mito, H., Bhatt, H. C., Bhatt, B. C. 2005, *MNRAS*, **358**, 1290.
Patel, M. K., Pandey, J. C., Savanov, I. S., Prasad, V., Srivastava, D. C. 2013, *MNRAS*, **430**, 2154.
Patten, B. M., Simon, T. 1996, *ApJS*, **106**, 489.
Pickles, A., Depagne, E. 2010, *PASP*, **122**, 1437.
Pizzolato, N., Maggio, A., Micela, G., Sciortino, S., Ventura, P., D'Antona, F. 2000, Proceedings from ASP Conference, Vol. 198., edited by R. Pallavicini, G. Micela & S. Sciortino, ISBN: 1-58381-025-0, 71.
Preibisch, T. 1997, *A&A*, **324**, 690.
Preibisch, T., Feigelson, E. D. 2005, *ApJS*, **160**, 390.
Preibisch, T., Kim, Y.-C., Favata, F., Feigelson, E. D., Flaccomio, E., Getman, K., Micela, G., Sciortino, S. *et al.* 2005, *ApJS*, **160**, 401.
Press, W. H., Teukolsky, S. A., Vetterling, W. T. *et al.* 1992, Numerical recipes in FORTRAN. The art of scientific computing.
Sagar, R., Munari, U., de Boer, K. S. 2001, *MNRAS*, **327**, 23.
Schmitt, J. H. M. M., Liefke, C. 2004, *A&A*, **417**, 651.
Scholz, A., Coffey, J., Brandeker, A., Jayawardhana, R. 2007, *ApJ*, **662**, 1254.
Siess, L., Dufour, E., Forestini, M. 2000, *A&A*, **358**, 593.
Skiff, B. A. 2007, yCat, 102023S, available at VizieR On-line Data Catalog http://webviz.u-strasbg.fr/viz-bin/VizieR.
Slesnick, C. L., Hillenbrand, L. A., Massey, P. 2002, *ApJ*, **576**, 880.
Smith, R. K., Brickhouse, N. S., Liedahl, D. A., Raymond, J. C. 2001, *ApJ*, **595**, 365.
Stassun, K. G., Ardila, D. R., Barsony, M., Basri, G., Mathieu, R. D. 2004, *AJ*, **127**, 3537.
Stelzer, B., Huélamo, N., Micela, G., Hubrig, S. 2006, *A&A*, **452**, 1001.
Stern, R. A., Zolcinski, M. C., Antiochos, S. K., Underwood, J. H. 1981, *ApJ*, **249**, 647.
Strom, S. E., Wolff, S. C., Dror, D. H. A. 2005, *AJ*, **129**, 809.
Strüder, L. *et al.* 2001, *A&A*, **365**, 18.
Turner, M. J. L. *et al.* 2001, *A&A*, **365**, 27.
Vaiana, G. S. *et al.* 1981, *ApJ*, **245**, 163.

Vuong, M. H., Montmerle, T., Grosso, N., Feigelson, E. D., Verstraete, L., Ozawa, H. 2003, *A&A*, **408**, 581.
Wade, G. A., Drouin, D., Bagnulo, S., Landstreet, J. D., Mason, E., Silvester, J., Alecian, E., Böhm, T. *et al.* 2005, *A&A*, **442**, 31.
Zhekov, S. A., Palla Francesco 2007, *MNRAS*, **382**, 1124.